Geochemical systematics of Pb isotopes, fluorine, and sulfur in melt inclusions from São Miguel, Azores

Estelle F. Rose-Koga, K.T. Koga, M. Moreira, Ivan Vlastélic, M.G. Jackson, M.J. Whitehouse, N. Shimizu, N. Habib

Geochemical systematics of Pb isotopes, fluorine, and sulfur in melt inclusions from São Miguel, Azores

EF Rose-Koga[1], KT Koga[1], M Moreira[2], I Vlastelic[1], MG Jackson[3], MJ Whitehouse[4], N Shimizu[5], N Habib[6]

(1) Laboratoire Magmas et Volcans, Université Blaise Pascal - CNRS - IRD, OPGC, 6 Avenue Blaise Pascal, 63178 Aubière, France
(2) Laboratoire de Géochimie et Cosmochimie, Institut de Physique du Globe de Paris, Sorbonne Paris Cité, Univ. Paris Diderot, UMR 7154 CNRS, 1 rue Jussieu, 75238 Paris, France
(3) University of California Santa Barbara, Department of Earth Science, Santa Barbara, CA, 93109-9630, USA
(4) Swedish Museum of Natural History, Box 50 007, SE-104 05 Stockholm, Sweden
(5) Woods Hole Oceanographic Institution, Dpt Geology & Geophysics, MA, USA
(6) UFR LACC, Université Blaise Pascal, Clermont-Ferrand, France

Abstract

Pb isotopic measurements in olivine-hosted melt inclusions of ocean island basalts (OIBs) from São Miguel, Azores, reflect the high $^{207}Pb/^{204}Pb$ and $^{208}Pb/^{204}Pb$ at a given $^{206}Pb/^{204}Pb$ of their host lavas. The data are consistent with a mixture between two endmembers: the first (the Central Group) has relatively high $^{208}Pb/^{206}Pb$ and is similar to the component sampled by Graciosa and Faial, and the second is a radiogenic endmember (with low $^{208}Pb/^{206}Pb$) that we refer to as the Nordeste component. F and Cl concentrations measured in the same melt inclusions from São Miguel represent parental abundances unmodified by crustal assimilation. Based on undegassed F and Cl concentrations, the source beneath São Miguel is volatile-rich. Among melt inclusions, Pb-isotope compositions correlate positively with S concentrations: we attribute this correlation to the dissolution of oceanic crust sulfides in the S-undersaturated basaltic melt of the Nordeste component. The blebs were assimilated by São Miguel magma and the magma droplets were later trapped in olivines.
When comparing melt inclusions from worldwide OIBs representing mantle endmembers, we find a global negative correlation between F/Nd and $^{208}Pb/^{206}Pb$ of volcanic glasses and melt inclusions. The high F/Nd (up to 40) endmember is represented by HIMU melt inclusions and the low F/Nd (down to 14) by EM1 Pitcairn glasses. São Miguel melt inclusions have an intermediate F/Nd = 23.1±3.4.

Keywords: melt inclusions, Pb isotopes, F/Nd, halogen, volatile elements, São Miguel

1. Introduction

The Azores archipelago comprises nine hotspot-related volcanic islands in the northern Atlantic, and a mantle plume has been resolved under the islands (French and Romanowicz, 2015). The geochemistry of Azores lavas is well documented (e.g. White et al., 1979; Schilling et al., 1980; Widom and Shirey, 1996; Turner et al., 1997; Moreira et al., 1999; 2012; Widom, 2002; Widom and Farhquar, 2003; Beier et al., 2007; Elliott et al., 2007).

Previous studies have used helium isotopes to identify three groups of islands in the Azores: the "Central Group" (with Terceira, Pico, and São Jorge) has the most "primitive" helium signature (i.e. low $^4He/^3He$, down to 39,200; R/Ra=18.4), the eastern group has radiogenic helium (with São Miguel, $^4He/^3He > 140{,}000$; $R/Ra < 5.1$), and the western group has a mid ocean ridge basalt--like (MORB)helium signature (i.e. $^4He/^3He$ around 88,000±5000; R/Ra=8; e.g. Moreira et al., 1999; 2012). Additionally, halogen concentrations are latitudinally graded from 30 to 50°N, crossing the Azores and the Mid-Atlantic Ridge (MAR), and a Cl-, Br-, and F-rich component was identified beneath the Central Group and the nearby ridge (Schilling et al., 1980). Recently, a water-rich mantle domain was proposed as the source of lavas from Pico (Métrich et al., 2014).

São Miguel is the largest and easternmost island of the Azores. Additionally, São Miguel is possibly one of the oldest islands in the archipelago (up to 4 Ma; Abdel-Monem et al., 1975; Moore, 1990), although this age of 4 Ma is debated (Johnson et al., 1998). Based on trace element concentrations and stable and radiogenic isotopic compositions, there is now a consensus among geochemists that the lavas from São Miguel represent a mixture between two endmembers: one with a HIMU-like Pb isotope composition (also found in São Jorge; Millet et al., 2009) and the second with a less radiogenic Pb isotopic composition common to the other islands of the Central Group (Widom and Shirey, 1996; Turner et al., 1997; Widom, 2002; Widom and Farhquar, 2003; Beier et al., 2007). The HIMU-like endmember has been argued to result from underplated basalt intruded into oceanic lithospheric mantle (Elliott et al., 2007) or from recycled material such as oceanic crust to which a small amount of evolved melt is added (<5%; Beier et al., 2007). A recent study combining helium and neon isotopes presented strong evidence for a recycled mafic magma as the origin of the HIMU component in the Azores (Moreira et al., 2012), corroborating the two previous studies.

However, with the exception of He and Ne, little data are reported for the volatile element characteristics of the São Miguel lavas (Moreira et al., 1999; 2012). Our study investigates the presence (or absence) of a Cl- and F-rich component in the mantle source under São Miguel, which would complement the existence of such a component beneath the Central Group (Schilling et al., 1980). We report new volatile element concentrations and Pb-isotopic data in olivine-hosted melt inclusions from São Miguel lavas. We identify a correlation between Pb-isotopes and S concentrations in the melt inclusions, and we attribute this correlation to the dissolution of sulfides (most likely of crustal origin) in a S-undersaturated

basaltic melt. Thus, this correlation demonstrates the role of sulfide in controlling the Pb-isotope composition in São Miguel inclusions. The volatile characteristics (Cl/K_2O and F/Nd) of the São Miguel parental magma are compared to hotspot mantle endmembers such as HIMU (Mangaia), enriched mantle I (EMI, Pitcairn), and enriched mantle II(EMII, Samoa). We show that olivine-hosted melt inclusions and submarine volcanic glasses from OIBs representing mantle endmembers have F/Nd that correlates with Pb-isotopes, and shows high F/Nd in the source of HIMU lavas and low F/Nd in the source of EMI and MORB lavas.

2. Sample description

The Azores Plateau is situated in the vicinity of the triple junction formed by the MAR and the ultraslow Terceira spreading axis (2–4 mm/a; Vogt and Jung, 2004). São Miguel, located 125 km west of the easternmost island, is host to five volcanic systems (from west to east): Sete Cidades, Picos, Fogo, Furnas, and Nordeste (Fig. 1). The oldest subaerial eruption unit is at the base of Sete Cidades. The Fogo (~200 ka) and Nordeste lavas (780-880 ka) are found below Furnas, which has lavas as old as 93 ka (Johnson et al. 1998). In this study, we examine olivine-hosted melt inclusions from six lavas of São Miguel. Whole rock sample descriptions have been provided in previous studies (Moreira et al., 1999; 2012): one sample (ACO95-03) is from the 1563 historical Queimado peak basanitoid lava flow in the Fogo volcanic system, four samples (ACO95-62; ACO95-68; 2000-4; 2000-9) are Nordeste ankaramites, and the sixth sample (ACO95-56) is from the Picos volcanic system.

3. Methods

3.1 Melt inclusion homogenization procedure

Helium isotope compositions of olivine phenocrysts from these six samples have been documented, and a subset analyzed for neon isotopes (Moreira et al. 1999; 2012). From these six rocks, we measured 19 olivine-hosted melt inclusions for Pb isotopes and volatile element concentrations (F, S, and Cl), and H_2O and CO_2 were measured on 9 of these inclusions. All melt inclusions were crystalline and required homogenization to generate glassy textures for analysis. Details of sample preparation procedures, including homogenization methods, are described elsewhere (Le Voyer et al., 2008, 2010). In brief, homogenization was performed on a Vernadsky-type heating stage. In order to both avoid oxidation of the host mineral and improve the quench rate, the oxygen fugacity was kept between 10^{-10} and 10^{-9} atm using He

that is purified with Zr at 700°C. The melt inclusions were heated until the last daughter mineral disappeared, kept at this "homogenization temperature" for 5 additional minutes, and then quenched. The homogenization procedure lasted 25 minutes total and the homogenization temperature was 1200±15ºC (see Le Voyer et al., 2008, 2010 for details on the homogenization procedure, and a volatile loss assessment in the supporting material of Cabral et al., 2014). Olivines spent less than 5 minutes above 1200ºC in the heating stage, preventing any significant H_2O loss from the melt inclusion, as shown in a prior study using the same heating stage at Clermont-Ferrand (Chen et al., 2011). Melt inclusions were exposed and polished individually, first on silicon carbide then with diamond paste of decreasing granular sizes (6, 3, and 1 μm). All polished inclusion-bearing olivines were pressed into a one-inch high-purity indium mount and polished with a ¼ μm alumina paste for 5 min to remove all scratches from the exposed surface of the glassy melt inclusions. The mount was then washed in an ultrasonic bath of pure ethanol for 10 min and then in distilled water for 10 min. The mount was dried in an oven at 100°C for at least 24 hours before final gold-coating. Prior to analysis, the mount was placed for at least 12 hours under high vacuum ($\sim 10^{-8}$ Torr) to reduce surface adsorption of volatile elements.

3.2 Standards and calibration for SIMS Pb-isotope measurements

The Pb isotope ratios were measured by secondary ion mass spectrometry (SIMS) on the multicollection SIMS 1280 located at the National Museum of National History (NMNH) in Stockholm, Sweden.

Repeat $^{207}Pb/^{206}Pb$ measurements of GOR132 glass standard (19 ppm Pb; Jochum et al., 2006) and R124 (homogeneous Reunion island glass; 2 ppm Pb) yielded errors of 0.40% and 0.96% (2 sigma), respectively (95% confidence interval; Fig. 4). A brief summary of the ion probe settings for Pb isotopic analysis follows. Prior to analysis, a 90 second pre-sputter with a 25 x 25 μm raster cleaned the surface of the sample. After the pre-sputter, the raster was stopped for analyses. During analysis, a focused O^{2-} primary beam of 8 nA sputtered the sample, with a primary accelerating voltage of 13 kV. We used a Kohler illumination method that resulted in a 15 μm flat-bottomed pit centered in the 25 μm square raster-cleaned area. Secondary positive ions were accelerated at 10 kV and analyzed at mass resolution of 4800 to avoid any mass interference. The size of the field aperture was set at 4000 μm, and the contrast aperture

at 400 μm. The centered energy window was adjusted to ±45 eV. The multicollection system was composed of 5 ion-counting electron multipliers set on moveable trolleys (L2, L1, C, H1 and H2). The detection array was configured to measure $^{204}Pb^{+}$ in the electron multiplier set on the trolley position L2, $^{206}Pb^{+}$ in L1, $^{207}Pb^{+}$ in C (placed on the ion optical axis) and $^{208}Pb^{+}$ in H1. The measurements were conducted over 40 to 120 cycles with a 20 s counting time for each mass and a deadtime correction of 60 ns. A measurement lasted approximately 20 min for 40 cycles. With this setting, the sensitivity on ^{208}Pb is 19 cps/ppm/nA (e.g. Rose-Koga et al., 2012; Rose-Koga et al., 2014).

A detailed description and discussion regarding Pb isotope measurements by multicollection SIMS is found in the supporting material of a previous study (Rose-Koga et al., 2012), where we analyzed the Pb-isotopic compositions of several standards with a wide range of SiO_2 concentrations (46 to 76 wt. %). The set of standards analyzed have dissimilar matrices, and the measured Pb isotope compositions did not suggest a matrix dependent mass fractionation. The trend formed by the standard data in Pb isotope space has a slope that is generally consistent with mass dependent fractionation (for details see Rose-Koga et al., 2012; supp. Material).

3.3 Volatile, major, and trace element analysis

Volatile element concentrations (H_2O, CO_2, F, S, and Cl) were measured by monocollection SIMS on the Cameca 1280 at WHOI (Woods Hole Oceanographic Institution, USA) on 11 melt inclusions. F, S, and Cl were measured by Electron Micro Probe (EMP) at LMV (Laboratoire Magmas et Volcans, France) on the remaining melt inclusions. The mono-collection SIMS settings employed here are standard and described elsewhere (Rose-Koga et al., 2008; Supplementary Table S5 in Helo et al., 2011; Rose-Koga et al., 2012). In short, we used a Cs^{+} primary beam with a current of 1.5 nA and an electron gun to compensate for charge build-up at the sample surface. After a 3 minute pre-sputtering with 30 x 30 μm square raster, analyses were performed on the central 15 μm spot centered in the rastered area by a mechanical aperture placed at the secondary ion image plane. The mass resolving power of 6600 allowed complete discrimination of interferences ($^{34}S^{1}H$ on ^{35}Cl, ^{17}O on $^{16}O^{1}H$, $^{29}Si^{1}H$ on ^{30}Si and $^{31}P^{1}H$ on ^{32}S). We used a critical illumination method, a 400 μm contrast aperture and a ±30 eV energy slit opening. Each measurement lasted approximately 15 minutes. The maximum uncertainties on the ion probe dataset, taking into account the reproducibility over

10 cycles of analyses and the uncertainties on the regression of the calibration line, were less than 5% for H_2O, 15% for CO_2, and 10% for Cl, F, and S (1σ).

Major elements were measured by EMP (Cameca SX 100 at LMV, France) in all melt inclusions, using standard procedures outlined in Le Voyer et al. (2008). F, S, and Cl were also measured by EMP at LMV on 9 melt inclusions. Cl, S, and F analyses were performed at 80 nA and with a 5 to 20 μm defocused beam together with the trace element acquisition program proposed in the Cameca Peak Sight software. The analytical standards were: natural scapolite for the Cl *K*α line, fluorite for F *K*α, and VG-2 glass for S *K*α. The sulfur concentration in VG-2 glass is assumed to be 1340 ppm; this value corresponds to the average of a compilation of published data (Dixon *et al*. 1991; Thordarson *et al*. 1996). Chlorine and sulfur were analyzed successively by using a large pentaerythritol (LPET) crystal and F was analyzed using a thallium acid phtalate (TAP) diffraction crystal. With 15 kV accelerating voltage and 80 nA beam current, counting time of 100 sec (Cl and S) and 600 sec (F), detection limits for S, Cl, and F were ~35, 50, and 200 ppm, respectively. The total analytical error for S, Cl, and F including precision and accuracy of measurements, was 20% (relative uncertainty) for S and 30% for Cl and F over the range of concentrations in our inclusions (Rose-Koga et al., 2008). Repeat analyses of standard VG-2 for F, S, and Cl gave values of 597±49, 130±11, and 210±10 ppm (±1σ), respectively.

Trace element measurements were carried out at LMV using a laser ablation system (193 nm Excimer Resonetics M-50E) coupled with an Agilent 7500 cs inductively coupled plasma mass spectrometer (LA-ICPMS). A laser spot size of 33 microns was used. Analyses were made with a laser pulse frequency of 2 Hz with a maximum output energy of 6 mJ. Twenty masses were collected with an integration time of 20 ms per mass: ^{85}Rb, ^{88}Sr, ^{89}Y, ^{90}Zr, ^{93}Nb, ^{137}Ba, ^{139}La, ^{140}Ce, ^{143}Nd, ^{145}Nd, ^{146}Nd, ^{147}Sm, ^{153}Eu, ^{157}Gd, ^{163}Dy, ^{166}Er, ^{178}Hf, ^{204}Ta, ^{232}Th, and ^{238}U. The internal reference mass was ^{44}Ca, where the CaO concentrations were measured by electron microprobe. A typical signal acquisition started by collecting a background signal for 30 seconds followed by a laser firing for 70 seconds or less, depending on the thickness of the melt inclusion. NIST 610 glass was used as an external standard. NIST 612 and BCR-2G glasses (Gao et al, 2007) were also analyzed to check the accuracy and precision of the analyses. Relative 1σ standard errors are better than 3% for Rb, Sr, Y, Zr, Nb, Ba, La, and Ce, less than 4% for Nd, better than 9% for Sm, Eu, Gd, Dy, Er, Hf, Ta, Th, and U, and 12% for Yb.

200

201

202 **4. Results**

203 Volatile element abundances and Pb isotope compositions are reported in Table 1 and major
204 element concentrations in Table 2. Trace element abundances are reported in Table 3.

205 *4.1. Major and trace element compositions*

206 The forsterite contents (mol %) of the host olivines range from 77 to 89. Within each olivine
207 grain, there are less than 0.7% relative variations of major element concentrations based on 2
208 to 3 electron microprobe analyses of each grain, indicating a lack of significant intra-grain
209 compositional heterogeneity. Crystallization of olivine from the wall of the melt inclusion
210 after entrapment changes the major and trace element composition of the melt inclusion. This
211 is a reversible process that is corrected for during the homogenization procedure and
212 correction for post-entrapment olivine overgrowth (also called Post Entrapment
213 Crystallization, PEC). This correction dissolves (or crystallizes) increments of equilibrium
214 olivine into the melt inclusion liquid until the Fe-Mg K_D reaches the equilibrium value (0.3;
215 Toplis, 2005). The mass fractions of olivine added to the inclusions in this correction
216 procedure were less than 13% of the melt for all but 2 inclusions, which required 16 and 20%
217 olivine correction (9/1/00 and ACO95-56a, respectively; Suppl. Material). SiO_2
218 concentrations of the corrected melt compositions range from 42 to 53 wt. %. The olivine
219 correction contributes negligible changes to the SiO_2 concentrations, as the range in SiO_2
220 before correction was 42 to 52 wt. % and the melt inclusions with extreme SiO_2
221 concentrations before correction remain the extreme ones after correction. The correction
222 mostly affects MgO concentrations of the melt inclusions: MgO before correction varies from
223 6.42 to 17.2 wt. %, and after correction between 3.17 and 15.5 wt. %. In a plot of total alkali
224 versus SiO_2, the melt inclusion corrected compositions fall in the fields of tephrite basanite,
225 basalt, trachy-basalt, and basaltic trachy-andesite. These compositions overlap with the whole
226 rock compositions of the mafic magmatic series of Saõ Miguel (Fig. 2).

227 Compared to a typical MORB, trace element abundances in the melt inclusions show a light
228 rare earth element (LREE) enriched pattern (Fig. 3a). Separate melt inclusions plot
229 essentially parallel to each other in the spidergram. REE patterns of Pico melt inclusions
230 overlap with those of São Miguel melt inclusions (Fig. 3a). By plotting all analyzed lithophile

trace elements in an approximate compatibility order for MORB, significant enrichment of the most incompatible elements (e.g., Rb, Ba, Th, U and Nb) is also apparent (Fig. 3b). The São Miguel melt inclusions have average Ba/La = 10.0±1.1, 11% relative standard deviation. The Ba/La for São Miguel whole rocks (Georoc database filtered for mafic lavas: 42 < SiO_2 < 53 wt. %) is statistically the same (10.9±1.8), attesting to the similarity between the spidergram patterns of whole rocks and melt inclusions. Similarly, the ratio of an incompatible element and a moderately incompatible element, Sr/Yb, gives values of 278±88 and 325±88 for the São Miguel whole rocks and melt inclusions, respectively.

4.2. Pb isotope compositions

In Pb isotope space, São Miguel (i.e., Nordeste component) whole rocks display a different trend compared to the Central Group ($^{206}Pb/^{204}Pb$ vs $^{208}Pb/^{204}Pb$; Fig. 5 insert), and the rocks from which we picked the olivines in this study represent extreme compositions of the Nordeste component: they come from samples with among the highest $^{208}Pb/^{204}Pb$ from São Miguel (between 40.05 and 40.45, inset of Fig. 5; ACO95-03, -56, -62, and -68). The trend of melt inclusions extends towards lower $^{207}Pb/^{206}Pb$ values than those reported in the literature for the whole rocks. However, it should be cautioned that the size of external reproducibilities of standards is comparable to the range of Pb isotope variability in melt inclusions observed in samples ACO95-68 and ACO95-03, suggesting that the isotopic heterogeneity found within these rocks are statistically insignificant (Fig. 4). The $^{208}Pb/^{206}Pb$ and $^{207}Pb/^{206}Pb$ variability found in samples ACO95-56 and ACO95-62, on the other hand, exceeds analytical uncertainty (2σ). Sample ACO95-62 shows $^{208}Pb/^{206}Pb$ variations at nearly constant $^{207}Pb/^{206}Pb$, whereas $^{208}Pb/^{206}Pb$ and $^{207}Pb/^{206}Pb$ variations are positively correlated in sample ACO95-56. Nevertheless, we stress that the general trend formed by the melt inclusions in a $^{207}Pb/^{206}Pb$ versus $^{208}Pb/^{206}Pb$ diagram (Fig. 5) is in good agreement with previous São Miguel literature data for whole rock lavas (e.g. Davies et al., 1989; Turner et al., 1997; Widom et al., 1997; Moreira et al., 1999; Elliott et al., 2007; Beier et al., 2007). ^{204}Pb normalized ratios vary within the analytical uncertainty of the measurements, and in $^{208}Pb/^{204}Pb$ vs $^{206}Pb/^{204}Pb$ isotopic space, the variation of the whole rock data plot along a ^{204}Pb error line (not shown). Therefore, it is not possible to identify statistically significant isotopic variation among the São Miguel melt inclusion samples in ^{204}Pb normalized isotope space, and ^{204}Pb normalized data are not shown in the figure.

4.3. Volatile element concentrations

H_2O and CO_2 concentrations in the São Miguel melt inclusions are lower than those reported for primitive melt inclusions from oceanic lavas at other localities. In recent melt inclusion studies, H_2O and CO_2 contents are routinely corrected for the fluid-phase bubble that is present in melt inclusions (e.g. Shaw et al., 2008, 2010; Koleszar et al., 2009). However, the volatile element concentrations are not corrected in this study, because the size of the bubble (when present) was not systematically measured prior to polishing the melt inclusions. The data display a large range of H_2O concentrations (from 107 to 1552 ppm) that are lower than those in melt inclusions from neighbouring Pico island (4000 to 21000 ppm; Métrich et al., 2014). Indeed, from the perspective of oceanic hotspot lavas, the São Miguel melt inclusions reported here have low H_2O concentrations. São Miguel melt inclusions average 900ppm H_2O, up to 12 times lower than some MORB glasses (between 1000 and 5200 ppm; e.g. Shimizu unpublished Famous MI data, Shaw et al., 2010; 800-11000 ppm; Le Voyer et al., 2015; Shimizu et al., 2016).

Relatively low CO_2 concentrations, ranging from 77 to 1178 ppm, accompany the low H_2O contents of São Miguel melt inclusions. The CO_2 abundances are in the lower range of that reported for the melt inclusions of Pico Island (697 to 4039 ppm), but are similar to the range of CO_2 in Mid Atlantic Ridge Lucky Strike melt inclusions (153 to 1498 ppm; Wanless et al., 2015).

Chlorine abundances in our melt inclusions are between 335±7 to 966±43 ppm (Fig. 6), and are comparable to Pico melt inclusions (330 to 900 ppm; Métrich et al., 2014; Fig. 6). Unlike many melt inclusions from oceanic lavas, Cl does not correlate with K_2O or other trace elements (e.g., Nb) that are similarly incompatible.

F concentrations in the melt inclusions vary from 637±98 to 1399±10 ppm (Fig. 6), comparable to the melt inclusions from Pico Island (742 to 1442 ppm; Métrich et al., 2014). F and K_2O concentrations correlate positively. The F/K_2O ratios of São Miguel melt inclusions are identical to those of Pico melt inclusions (336 and 332, respectively). These values are higher than Atlantic MORB glasses (71 to 519 ppm; Le Voyer et al., 2015). The F concentrations in Azores melt inclusions resemble those of Samoan submarine glasses (818 to 1887 ppm; Workman et al., 2006), and the range extends to higher values than in olivine-hosted melt inclusions from hotspot basalts such as the Yellowstone hot spot (55 to 977 ppm;

293 Stefano et al., 2011). Extreme HIMU melt inclusions from Mangaia have generally higher F
294 concentrations (1180 to 1950 ppm; Cabral et al., 2014; Fig. 6).

295 S concentrations in São Miguel melt inclusions are between 311±34 and 2115±56 ppm
296 (Table 1). Sulfur is usually considered to be incompatible in silicate minerals, but shows no
297 consistent trend with other incompatible elements in São Miguel melt inclusions. S
298 concentrations in São Miguel melt inclusions decrease with decreasing FeO concentration.
299 The range of S concentrations in São Miguel melt inclusions overlaps with that of melt
300 inclusions from Pico Island (1195 to 1954 ppm; Métrich et al., 2014). São Miguel melt
301 inclusions are sulfide saturated (see Discussion, below); for comparison, Pico melt inclusions
302 are also described as sulfide saturated (Métrich et al., 2014).

303

304 **5. Discussion**

305 *5.1. Assessment of parental magma compositions from São Miguel melt inclusions*

306 The olivine-hosted melt inclusions in this study represent parental magmas of the São Miguel
307 lavas. First, host-olivines found in basaltic lavas are generally forsteritic (77 to 89, with an
308 average of 84). Second, trace element patterns (Fig. 3a) lack pronounced Sr and Eu
309 anomalies, and the small negative anomalies in Ba and Sr do not correlate with Al_2O_3, Na_2O,
310 or CaO, indicating only minor (if any) plagioclase fractionation, and suggesting no crustal
311 assimilation took place (Fig. 3a). Significant plagioclase fractionation or assimilation in the
312 underlying oceanic crust is therefore unlikely. Because of the forsteritic host-olivine
313 compositions and the lack of significant crustal modification, we conclude that these melt
314 inclusions were trapped at an early stage of crystallization from a little-modified, mantle-
315 derived primitive magma.

316 Compositional corrections for post-entrapment crystallization and degassing of melt
317 inclusions are viable only for inclusions that did not experience diffusive exchange with the
318 magma surrounding the host olivine. In reality, the host olivine can continuously exchange Fe
319 and Mg with the surrounding magma, potentially leading to Fe-loss from melt inclusions.
320 Therefore, exact reconstruction of the FeO and MgO content of the parental magma cannot
321 be achieved (Danyushevsky et al., 2000; 2002; Gaetani and Watson, 2000). However, the
322 ratios of incompatible trace elements remain unmodified as they are not partitioned into
323 olivine, and are therefore representative of the primitive parental magma. Note that the trace

element and REE patterns of the São Miguel melt inclusions are roughly parallel and tightly distributed (Fig. 3a,b), and Ba/La and Sr/Yb ratios of whole rocks and melt inclusions are statistically indistinguishable.

The REE patterns of São Miguel and Pico melt inclusions overlap (Fig. 3a). Since Sr and Yb have different compatibilities during mantle melting, the lack of variation of Sr/Yb ratios in both São Miguel (286±87) and Pico (244±43) melt inclusions indicates that the primitive magmas of the islands are derived from comparable degrees of partial melting of a similar initial lithology. Furthermore, the lack of variation of Ba/La (10±1 for São Miguel and 9±1 for Pico), a ratio of two highly incompatible elements, indicates that the magmas were derived from a similar initial bulk lithology.

Here, the term "initial lithology" represents the material prior to melting. It is used to distinguish from the term "magma source". The latter refers to isotopically distinct entities that are involved in the magma genesis (in particular, Pb isotopes in this study). Thus, the trace element similarity between Pico and Saõ Miguel whole rocks suggest the presence of a single dominant initial lithology with similar bulk chemistry (e.g. White et al., 1979; Turner et al., 1997; Elliott et al., 2007; Beier et al., 2007). However, there exist distinct magma sources that contribute to the observed isotopic variations (e.g. Davies et al., 1989; Kurz, 1993; Turner et al., 1997; Moreira et al., 1999; Widom et al., 1996, 1997, 2003).

It should be noted that these melt inclusion samples are hosted in whole rocks that span a range of ages (300 ky to present) and geographical locations (55 km east-west on São Miguel). The similarity of trace element characteristics among São Miguel whole rock basalts has been noted in previous studies (White et al., 1979; Elliott et al., 2007; Beier et al., 2007), and the melt inclusion trace element data presented here corroborate earlier observations. The similarity of parental magmas can be extended geographically to other volcanoes on different islands of the Azores archipelago. Several previous whole rock studies noted nearly identical trace element characteristics among Faial, Pico, and São Jorge (White et al., 1979; Turner et al., 1997; Beier et al., 2007, 2012). It appears that, based on major and trace element compositions of basalts and melt inclusions, the mantle beneath these Azores islands must have a similar lithology to generate such similar trace element patterns, with geodynamic conditions permitting the production of uniform degrees of partial melting.

354 *5.2. Volatile element characteristics of São Miguel melt inclusions*

355 5.2.1. "Lost" volatiles: H_2O and CO_2

356 The parental magma beneath São Miguel records the lowest degree of partial melting in the
357 archipelago (<4%; Bourdon et al., 2005), allowing the extracted melt to be richer in H_2O
358 compared to typical MORB (0.1–0.5 wt. % H_2O in MORB; Michael, 1988; Dixon and
359 Stolper, 1995; Sobolev and Chaussidon, 1996). Furthermore, a greater H_2O abundance in the
360 initial Azores mantle compared to that of MORB (e.g. 116 ppm Salters and Stracke, 2004)
361 would favor the generation of wet magma. Previous estimates of H_2O abundance in the
362 Azores mantle plume range between 200 ppm (based on melting temperatures and pressures
363 determined by mineral and lava compositions; Beier et al., 2012) and 700 ppm H_2O (based on
364 a pHMELTS model; Asimow et al., 2004). From melt inclusions, an estimate of 680 ppm
365 H_2O is modelled for the mantle beneath Pico Island (Métrich et al., 2014). Using the H_2O
366 content of the mantle beneath Pico Island, and given a degree of partial melting between 2.5
367 and 4% (Bourdon et al., 2005), the H_2O concentration of un-degassed São Miguel melt
368 inclusions could reach values from 1.7 to 2.7 wt. %. In this case, São Miguel melt inclusions
369 have lost up to 91% of their initial H_2O content. Here, the reported H_2O contents of São
370 Miguel melt inclusions represent minimum H_2O values, and do not represent either the initial
371 H_2O concentrations at the time of entrapment or the primitive H_2O abundance of the Azores
372 magma because hydrogen can diffuse from melt inclusions through the host olivine crystal
373 (Chen et al., 2011; Gaetani et al., 2012; Gaetani et al., 2014). An indicator of diffusive
374 hydrogen loss is the correlation of H_2O concentration and melt inclusion size (long or short
375 axis of the melt inclusion, Chen et al., 2011). This correlation is based on the fact that
376 diffusive hydrogen loss is promoted by the larger surface-to-volume ratios of smaller melt
377 inclusions. Among 5 melt inclusions in which H_2O was measured, we found a positive
378 correlation between their sizes (long axis L and short axis l, Table 2) and H_2O contents (R^2 =
379 0.90 and 0.93, respectively). Melt inclusions from this study have therefore most likely
380 suffered diffusive hydrogen loss through the host olivine. Henceforth, we will consider the
381 measured H_2O concentrations as being affected by H diffusion and representative of
382 minimum H_2O concentrations.

383 Like H_2O, CO_2 measurements represent minimum values. Bubbles are occasionally present in
384 melt inclusions, and such bubbles can contain CO_2. A "bubble correction" might not be
385 significant for H_2O (e.g. <2%; Shaw et al., 2008) but can reach non-trivial values for CO_2

(e.g. >80%; Shaw et al., 2008). Therefore, the CO_2 measurements in São Miguel melt inclusions represent minimum values, where most of the CO_2 has potentially degassed to the fluid-phase bubble. Additionally, CO_2 degasses from melt at a greater depth than other volatile elements, and the melt inclusions trapped by olivine at magma chamber depths are likely to have already degassed. This is supported by the observation that CO_2 concentrations correlate poorly with concentrations of refractory incompatible elements (not shown). Therefore the pressure derived from H_2O and CO_2 measurements (using MagmaSat v1.0; Ghiorso, 2015) does not represent the pressure of entrapment (Table 1). The highest entrapment pressure determined for São Miguel melt inclusions is 12MPa and we will use this extremely conservative minimum pressure only for discussion of the potential degassing of other volatile species. Confirmation of the presence or absence of a volatile-rich mantle beneath São Miguel requires constraints from other volatile systems that are less susceptible to diffusive loss from the melt inclusions.

5.2.2. Wet São Miguel mantle? Constraints from F and Cl

São Miguel melt inclusions are not degassed with respect to F (calculated pressures from Table 1 are higher than the degassing pressure of F, ≈10 MPa; Spilliaert et al, 2006). F concentrations correlate positively with K_2O concentration in São Miguel melt inclusions, showing that F is an incompatible element during magma evolution. In fact, F concentrations also generally correlate positively with other incompatible refractory trace elements (e.g. Rb, Sr, Ba, Nb), confirming that F was not lost while H_2O and CO_2 diffused from the melt inclusions.

The range of Cl concentrations in melt inclusions from Pico (350 to 900 ppm) and São Miguel (335 to 966 ppm) are identical within uncertainty. Cl can be degassed from erupted lavas, but we argue that Cl was not degassed from the São Miguel melt inclusions prior to entrapment. For example, the degassing pressure threshold for Cl in an H_2O-CO_2-rich alkali basalts of Mount Etna is ~100 MPa, and for F ~10 MPa (~140 MPa for S ; Spilliaert et al., 2006), illustrating the potential for shallow-level Cl degassing and even shallower-level F degassing. However, arc magmas such as Etna are rich in volatile elements, and the pressure thresholds for degassing of Cl and F should be lower for the relatively volatile-poor São Miguel melts.

In São Miguel melt inclusions, F and Cl are the two reliable volatile elements for evaluation of primary melt compositions. The SolEx model (Witham et al., 2012) is used to estimate an

418 open-system degassing curve for Cl (F is not feasible with SolEx), assuming the initial
419 undegassed melt contains 2 wt. % H_2O and 5100 ppm CO_2 (Pico melt inclusion compositions
420 from Métrich et al., 2014), 900 ppm Cl and 2100 ppm S (the maxima in this study). Model
421 results show that 99% of the initial Cl remains in the melt during magma ascent. Therefore, at
422 the time of melt entrapment, we consider that most of the magma has not significantly
423 degassed Cl or F.
424 To assess the origin of the undegassed Cl, and decipher if it is characteristic of the source or
425 assimilated materials, we employ the Cl/K_2O ratio as an indicator of assimilation of seawater
426 or seawater-derived materials by mantle melts (e.g. Lassiter et al., 2002). The Cl/K_2O ratio is
427 also easier to compare to other studies since K_2O measurements are readily available in the
428 literature (by comparison, less Cl/Nb data exist). Among OIB melt inclusions, Cl/K_2O in São
429 Miguel melt inclusions, and a few submarine Pitcairn glasses (Woodhead and Devey, 1993),
430 are among the lowest reported (Fig. 7): Cl/K_2O ratios are less than 0.05 in our São Miguel
431 inclusions, similar to values of pristine melt reported for the Austral Islands (Lassiter et al.
432 2002), and thus lower than the suggested 'cut-off' value of 0.05 for MORB (Michael and
433 Cornell, 1998; Shimizu et al., 2016). Above this value, melts are argued to have experienced
434 assimilation of seawater-derived materials, such as altered oceanic crust. Thus, we suggest
435 that there is no detectable assimilated Cl in the melt inclusions, and the Cl and K_2O
436 compositions represent those of the primitive melts.
437 Overall, Cl and F exhibit concentrations comparable to volatile element-rich inclusions from
438 Pico island. A subset of the São Miguel inclusions (excluding degassed samples) have
439 Cl/K_2O ratios in the range of Pico melt inclusions (Fig. 6). Furthermore, F/Nd values of Pico
440 melt inclusions are identical to F/Nd of São Miguel melt inclusions, and the relative trace
441 element abundances of melt inclusions from São Miguel and Pico also similar. Based on
442 these similarities, the mantle beneath São Miguel is inferred to be as volatile-rich as that
443 beneath Pico, and we propose that the volatile-rich mantle source of the Azores hotspot
444 (found under the MAR and Pico island) extends westward beneath São Miguel (e.g. Asimow
445 et al., 2004; Métrich et al., 2014).

446 5.2.3. Sulfur, iron and Pb isotope variations

447 The S concentrations of São Miguel melt inclusions correlate positively with FeO
448 (correlation coefficient =0.72; Fig. 8). Such a correlation is often interpreted as resulting from
449 sulfide saturation in the magma because S solubility increases with increasing FeO content

(e.g. Li and Naldrett, 1993; O'Neill and Mavrogenes, 2002). Several models are available for investigation of S saturation in São Miguel melt inclusions. Sulfide saturation in magmas can be determined with models parameterized for P, T, composition, and $f(O_2)$ (Wallace and Carmichael, 1992; more recent models, however, do not employ oxygen fugacity; Liu et al., 2007; Li and Ripley, 2009), as well as H_2O content (Fortin et al., 2015). Here, we use the model of Fortin et al. (2015) to determine sulfur concentration at sulfide saturation (SCSS) corresponding to the melt inclusions (T=1200ºC, and P calculated by MagmaSat with $f(O_2)$=QFM+1); note that for samples with no H_2O measurements, we assumed H_2O=1552 ppm, the maximum measured H_2O content in our São Miguel melt inclusions. The S saturation conditions are represented (Fig. 9) by an uncertainty band delimited by dotted lines, which represents a variation of ±50% around an ideal value, where the ideal value refers to the thermodynamic equilibrium value (see Fig. 6b of Fortin et al., 2015, in which ±50% was assessed by the relative difference between modelled S and measured S concentrations for natural samples with less than 2000 ppm S). Model results indicate that only two melt inclusions plot outside of the sulfide saturation band (ACO95-62i, its replicate measurement, and 2000-9-4). All other melt inclusions analysed follow a linear-trend parallel to the 1:1 line (Fig. 9). If the H_2O concentration (1552 ppm) is increased to 2 wt% (maximum H_2O concentration in Pico melt inclusions; Métrich et al., 2014), the modelled S concentrations of São Miguel melt inclusions increase by 20% but remain within the S saturation uncertainty band. If temperature is decreased to 1150ºC, the SCSS decreases by 13% and the São Miguel melt inclusions plot closer to the 1:1 line. Pressure is not a sensitive parameter in this model. Based on these calculations, sulfur concentrations in the majority of São Miguel melt inclusions are at sulfide saturation. The two sulfide-undersaturated melt inclusions have lower S concentrations (<400ppm). Therefore, the sulfur content of these S-undersaturated samples is likely controlled by degassing (i.e. sulfate formation), and not by sulfide saturation. The following discussion excludes these two S-undersaturated melt inclusions. The correlation between S concentrations and Pb isotopic compositions in the melt inclusions is enigmatic (Fig. 8). Here, the correlation implies a relationship between two geochemical processes: sulfide saturation (dissolution/precipitation) and the mixing of at least two distinct Pb-isotopic components. Because precipitation of sulfide within melt inclusions cannot account for this correlation, the isotopically distinct magma compositions must have been present prior to melt inclusion entrapment. Accounting for these conditions, we propose a scenario where sulfide blebs with unradiogenic Pb-isotopic compositions (high $^{207}Pb/^{206}Pb$)

483 dissolve to various extents into São Miguel melts before the melts are trapped in olivines.
484 Two critical assumptions are required for this model, which are the presence of (1) a sulfide-
485 undersaturated magma, and (2) Pb-rich sulfides with high $^{207}Pb/^{206}Pb$. The first assumption is
486 valid since the solubility of S increases with decreasing pressure (e.g. Fortin et al., 2015); the
487 S content of magma formed in the mantle will most likely be undersaturated at shallower
488 depth (for example in a magma chamber). For our second hypothesis, the existence of a high
489 $^{207}Pb/^{206}Pb$ signature in sulfide is not an exotic idea (e.g. Warren and Shirey, 2012) and high
490 values for Pb partition coefficients between sulfide and melt (e.g. Kiseeva and Wood, 2013;
491 Patten et al., 2013; Hart and Gaetani, 2016) now suggest some sulfides can have high Pb
492 concentrations. If such a S-undersaturated melt can interact with sulfides present in a
493 lithology predating the sulfide-understaturated magma (for example sulfides in the wall of the
494 magma chamber, genetically unrelated to the S-undersaturated magma), each with distinct Pb
495 isotope compositions, a mixing model can quantitatively test the amount of sulfide dissolved
496 into the magma. This sulfide dissolution process can generate variability in Pb
497 concentrations, S concentrations, and Pb isotopic ratios. A similar idea of oceanic crust (or
498 oceanic lithosphere)-sulfide dissolution/destabilisation has recently been proposed to explain
499 the disequilibrium of Pb isotopes between Fe oxides and their host rocks in Reunion Island
500 (Vlastélic et al., 2016). We apply a binary mixing model between a sulfide melt and a basaltic
501 magma. The sulfide endmember composition is chosen as FeS (36 wt. % S). The basaltic
502 magma composition has a concentration of 500 ppm S (corresponding to the minimum S
503 measured in São Miguel melt inclusions, excluding the degassed melt inclusion). The lead
504 isotope end members are $^{207}Pb/^{206}Pb$ =0.857 for sulfides (representing oceanic crust) and
505 $^{207}Pb/^{206}Pb$ =0.780 for the basaltic Nordeste component (the lowest $^{207}Pb/^{206}Pb$ value a melt
506 inclusion can reach; Table 1). Model results show the observed Pb-isotope and S
507 concentration variations in São Miguel melt inclusions are explained by less than 0.4% of
508 sulfide incorporation (Fig. 8; similar to the sulfide fraction proposed for Réunion island,
509 Vlastélic et al., 2016). The mixing proportion of sulfide is sufficiently low that major and
510 incompatible (and non-chalcophile) trace element compositions remain unchanged and
511 identical to the magma derived from the São Miguel mantle. However, this mixing will
512 change the Pb isotopic composition, S abundance, and the abundances of all chalcophile
513 elements, because Pb is a strongly chalcophile element in magmatic systems (e.g., Hart and
514 Gaetani, 2006; 2016; Kiseeva and Wood, 2015; Wood and Kiseeva, 2015).

Lead concentrations of the endmembers are derived as follows. Because Pb concentrations were not measured in this study, we estimated the range of Pb concentrations in the melt inclusions using Ce/Pb of São Miguel lavas (from 21 to 30: Georoc database, filtered for SiO_2 between 42 and 53 wt. %). From measured Ce concentrations, Pb concentrations in the melt inclusions are estimated to be between 2 to 6 ppm. A value of 2 ppm Pb is used for the modelled basaltic magma endmember to have a lower estimate of Pb concentration in sulfides. The sulfide endmember must have formed from a cooling magma at the time of oceanic crust formation. Therefore, the concentration of Pb in the sulfide is determined using a Pb partition coefficient ($D_{Pb}^{sulfide/melt}$) and a mantle derived basalt with 2 ppm Pb, and it ranges from 60 and 280 ppm Pb using $D_{Pb}^{sulfide/melt}$ of 30 and 140, respectively. These partition coefficients are determined by extrapolation of the parameterisation of Hart and Gaetani (2016). For comparison, $D_{Pb}^{sulfide/melt}$ values ranging from 45 to 73 were measured between sulfide droplets and coexisting natural MORB glasses (Patten et al., 2013) and the model of Kiseeva and Wood (2013) gives 25 to 98 depending on the measured FeO contents of our melt inclusions. Because $D_{Pb}^{sulfide/melt}$ is a function of pressure, where D is higher at low pressure, the oceanic crust sulfide with high Pb concentration is inferred to have formed at low pressure (< 0.5 GPa). It should be noted that low Pb abundances are found in sulfides from abyssal peridotites (average 4 ppm; Warren and Shirey, 2012), where sulfides are thought to form at high pressure (low $D_{Pb}^{sulfide/melt}$) before emplacement at the ocean floor.

Os is also a chalcophile element (e.g. Brenan, 2008), but Os isotopes show little variation in São Miguel lavas (Widom et al., 1996), perhaps because, unlike Pb, there is little Os isotopic variability between the Azores mantle plume and the dissolving sulfides. Since sulfide does not carry Sr or Nd, the sulfide dissolution model would not generate correlation of Pb isotopes with Sr and Nd isotopes. This sulfide dissolution model for our melt inclusion study could be in contradiction with previous observations of whole rock correlations of Pb-isotopes with Sr and Nd isotopes (e.g. Beier et al., 2007; Elliott et al., 2007). However, it has been suggested that Pb isotopes are de-coupled from Sr and Nd isotopes, which are more silicate-controlled isotopic tracers (e.g. Hart and Gaetani, 2006). Upon close inspection, the model of Beier et al. (2007) requires the presence of mafic material in both Central and Nordeste source mantles. Incorporation of our sulfide dissolution model into the model of Beier et al. (2007) would not cause a contradiction, supposing that the Pb isotopic composition of the Central Group mafic component is abundant in the oceanic crust sulfide.

We rule out other mixing hypotheses that could account for the correlation of S concentrations and Pb isotopes. For example, if magma mixing occurs between low FeO (evolved) and high FeO (primitive) magmas with different endmember Pb isotopic compositions, and if the melts were sulfide saturated, a correlation between FeO, S, and Pb isotopic ratios might be expected. However, this mixing scenario should lead to a linear correlation between every chemical component (e.g. major elements), a characteristic not observed in the São Miguel melt inclusion dataset.

5.3. F/Nd characteristics of melt inclusions from OIB magmas

It has been suggested that F/Nd in melt inclusions and glasses from MORB and OIB is relatively constant (average value of 21±5 from Workman et al., 2006) because there is no significant F/Nd fractionation during crystallization and melting. These two incompatible elements have similar bulk partition coefficients during mantle melting (e.g. Dalou et al., 2011). Hence, F/Nd is a canonical ratio that can be used to trace mantle sources. Specifically, using basalt–bulk peridotite partition coefficients, $D_F/D_{Nd} = 0.056/0.044 = 2.24$ (values from Dalou et al., 2014; and alphaMELTS default routine), the concentration ratio of F/Nd in the melt deviates less than 20% from the source ratio when the degree of partial melting exceeds 0.5%. An average of São Miguel melt inclusions gives F/Nd = 23.1±3.4 (1σ) (Figs. 7, 10). The relative constancy of the F/Nd value suggests that there is a single parental magma beneath São Miguel with F/Nd of 23.1±3.4. As was the case for other trace element ratios, F/Nd does not correlate with Pb isotopic compositions in the São Miguel melt inclusion suite.

Pb isotope compositions represent a classical geochemical tracer of mantle sources of hotspot lavas. Mantle endmembers such as HIMU (e.g. Mangaia), EMI (e.g. Pitcairn) and EMII (e.g. Samoa) are considered endmembers based on their extreme isotope compositions among hotspot lavas erupted globally (e.g. Zindler and Hart, 1986; Hofmann, 1997; White, 2015). F/Nd ratios in melt inclusions can potentially characterize the mantle source of melts, similar to Pb isotopic ratios. Therefore, comparing both F/Nd and Pb isotope measurements from different OIBs would illustrate F heterogeneity in the mantle. Fig. 10 shows a broad negative correlation between F/Nd and $^{207}Pb/^{206}Pb$ defined by melt inclusions and glasses from OIBs defining mantle endmembers, confirming that F/Nd records mantle heterogeneity (e.g. Lassiter et al. 2002; Koleszar et al., 2009; Rose-Koga et al., 2012; Jackson et al., 2015). For example, oceanic melts with radiogenic Pb-isotopic compositions (high $^{206}Pb/^{204}Pb$, or low $^{208}Pb/^{206}Pb$ and low $^{207}Pb/^{206}Pb$) tend to have elevated F/Nd ratios, and oceanic melts with less

radiogenic Pb-isotopic compositions (low $^{206}Pb/^{204}Pb$, or high $^{208}Pb/^{206}Pb$ and high $^{207}Pb/^{206}Pb$) tend to have lower F/Nd ratios. Mangaia melt inclusions, which have the most radiogenic (HIMU) Pb isotopic compositions globally, have relatively high F/Nd, between 20 and 40 (Cabral et al., 2014; Fig.7). São Miguel inclusions are consistent with this relationship: the slight HIMU signature of São Miguel melt inclusions is reflected by the relatively high F/Nd (18 to 27). São Miguel melt inclusions have F/Nd overlapping that of Samoa basaltic glasses (representative of EMII, Fig.10), consistent with the influence of an enriched endmember component in the source of São Miguel. EMI has lower F/Nd (between 14 and 20, represented by Pitcairn glasses; Fig. 8) that is similar to MORB.

The origin of the global relationship between F/Nd and Pb-isotopic compositions may relate to both (i) the recycled protoliths (oceanic crust, sediments, etc.) that are subducted and mixed into the mantle sources of different hotspots and (ii) the recycling efficiency of F. While F and Cl likely have elevated concentrations in a subducting slab (e.g. Straub and Layne, 2003; Debret et al., 2013), both are likely lost from the slab during dehydration or melting at subduction zones (Kendrick et al., 2011, 2012 for Cl; Kendrick et al., 2014 for F). If ancient subducted oceanic crust is responsible for the generation of radiogenic Pb isotopic reservoirs (e.g. HIMU) in the mantle (e.g. Hofmann and White, 1982; Hauri and Hart, 1993; Hanyu et al., 2011), then the elevated F/Nd in oceanic lavas with a radiogenic signature suggests that F is retained (with respect to Nd) in the slab during subduction. In contrast, oceanic lavas sampling the EMI and EMII reservoirs tend to have lower F/Nd, which suggests that the protoliths (pelagic sediments, terrigenous sediments, lower continental crust, etc.) were more efficiently stripped of their complement of F than the HIMU domain. The process that leads to different degrees of F retention relative to Nd during subduction is not well known, but must relate to variable F loss from the subducting slab, possibly as a function of different temperatures and bulk lithologies (sediments versus oceanic crust, etc.; see Van den Bleeken and Koga, 2015). Upon dehydration, the hydroxyl site in silicate minerals – which has a strong affinity for F (e.g., Smith et al., 1981; Wu and Koga, 2013) – provides an ideal mineralogical site to promote recycling of F. Thus, following prograde metamorphism, residual subducted mafic slab mineralogies with amphibole, mica, and/or apatite would be conducive to efficient transport of F into the deeper mantle with the downgoing slab. However, partial melting of the subducting slab sediments would promote efficient transport of F (along with Nd) to the mantle wedge, depleting the slab of its complement of F (e.g. Rose-Koga et al., 2014). Indeed, thermal models suggest the top

portion of the slab to be the hottest, and sediments have a lower solidus temperature than oceanic crust (e.g. Peacock, 1990; Van Keken et al., 2002). This model may help explain why enriched mantle reservoirs that host recycled sediments will be depleted in F (lower F/Nd), while HIMU mantle reservoirs hosting recycling oceanic crust will be less depleted in F (higher F/Nd).

6. Conclusions

São Miguel olivine-hosted melt inclusions suggest a single initial lithology beneath the island based on three lines of evidence. (1) The major element compositions of the inclusions cluster towards the low SiO_2 range of the entire São Miguel whole rock trend. (2) Trace element patterns are tightly clustered and parallel. However, despite this uniform trace element composition, variations in Pb isotopic compositions are interpreted following the scenario for the whole rock, as mixing between a non-radiogenic component, "the Central Group Component", and a radiogenic component called "the Nordeste Component". (3) Based on undegassed F and Cl, the source beneath São Miguel is volatile-rich, therefore the "wet" source beneath Pico island (Métrich et al., 2014) extends eastward under São Miguel.

The Pb-isotopic compositions of the melt inclusions correlate positively with S concentrations. This is tentatively interpreted as being due to small sulfide blebs (isotopically distinct with respect to Pb) located in the oceanic crust of the Central Group component that are dissolved by a S-undersaturated Nordeste component magma. This process does not significantly affect the major and trace element contents of the melt inclusions, but drastically modifies the Pb isotope compositions and S concentrations.

Refining the volatile element chemical characteristics of the melt inclusions, we defined characteristic $Cl/K_2O=0.035\pm0.011$ and $F/Nd=23.1\pm3.4$ for the parental magma of São Miguel island.

Comparing melt inclusions from OIBs representing mantle endmembers, we show a global negative correlation between F/Nd and Pb isotope composition of melt inclusions. São Miguel melt inclusions have intermediate F/Nd, between the lower F/Nd of Pitcairn melt inclusions (representing EMI, between 14 to 20) and the higher F/Nd of Mangaia melt inclusions (representing HIMU, between 20 and 41).

Acknowledgements: ER-K thanks JL Devidal for his precious guidance and discussions during the electron probe analysis. Many thanks go to ER & FR having often kept "distractions" away during the writing of this manuscript. Thank you to R. Dennen for

English editing (RD Editing Services). ER-K acknowledges financial support from the CNRS (Institut National des Sciences de l'Univers). This research was financed by the French Government Laboratory of Excellence initiative n°ANR-10-LABX-0006, the Région Auvergne and the European Regional Development Fund. MGJ acknowledges NSF grant EAR-1347377. This is Laboratory of Excellence ClerVolc contribution number XXX. The NordSIMS facility is financed and operated under a joint Nordic contract; this is NordSIMS contribution no. XXX.

References

Abdel-Monem, A. A., L. A. Fernandez and G. M. Boone, 1975, "K-Ar ages from the eastern Azores group (Santa Maria, São Miguel and the Formigas Islands)." Lithos, 8, 247-254.

Agranier, A., Blichert-Toft, J., Graham, D., Debaille, V., Schiano, P., and Albarede, F., 2005, The spectra of isotopic heterogeneities along the mid-Atlantic Ridge: Earth and Planetary Science Letters, 238, 96–109, doi: doi:10.1016/j.epsl.2005.07.011.

Asimow, P.D., Dixon, J.E., and Langmuir, C.H., 2004, A hydrous melting and fractionation model for mid-ocean ridge basalts: Application to the Mid-Atlantic Ridge near the Azores, Geochemistry Geophysics Geosystems, 5, doi: 10.1029/2003GC000568.

Beier, C., Haase, K.M., and Hansteen, T.H., 2006, Magma Evolution of the Sete Cidades Volcano, São Miguel, Azores: 47, 1375–1411.

Beier, C., Stracke, A., and Haase, K., 2007, The peculiar geochemical signatures of São Miguel (Azores) lavas: Metasomatised or recycled mantle sources?: Earth and Planetary Science Letters, 259, 186–199.

Beier, C., Haase, K., and Turner, S., 2012, Conditions of melting beneath the Azores: Lithos, 144-145, 1–11.

Bourdon, B., Turner, S.P., and Ribe, N.M., 2005, Partial melting and upwelling rates beneath the Azores from a U-series isotope perspective, Earth and Planetary Science Letters, 239, 42–56.

Brenan, J.M., 2008, Re–Os fractionation by sulfide melt–silicate melt partitioning: A new spin: Chemical Geology, 248, 140–165.

Bucholz, C.E., Gaetani, G.A., and Behn, M.D., 2013, Post-entrapment modification of volatiles and oxygen fugacity in olivine-hosted melt inclusions: Earth and Planetary Science Letters, 374, 145–155.

Cabral, R.A., Jackson, M.G., Koga, K.T., Rose-Koga, E.F., Hauri, E.H., Whitehouse, M.J., Price, A.A., Day, J.M.D., Shimizu, N., and Kelley, K.A., 2014, Volatile cycling of H 2O, CO 2, F, and Cl in the HIMU mantle: A new window provided by melt inclusions from oceanic hot spot lavas at Mangaia, Cook Islands: Geochemistry Geophysics Geosystems, 15, 4445–4467, doi: 10.1002/2014GC005473.

Chen, Y., Provost, A., Schiano, P., and Cluzel, N., 2011, The rate of water loss from olivine-hosted melt inclusions: Contributions to Mineralogy and Petrology, 162, 625–636, doi: 10.1007/s00410-011-0616-5.

Dalou, C., Koga, K.T., Shimizu, N., Boulon, J., and Devidal, J.-L., 2011, Experimental

687 determination of F and Cl partitioning between lherzolite and basaltic melt: Contributions to
688 Mineralogy and Petrology, 163, 591–609, doi: 10.1007/s00410-011-0688-2.

689 Danyushevsky, L., Della-Pasqua, F., and Sokolov, S., 2000, Re-equilibration of melt
690 inclusions trapped by magnesian olivine phenocrysts from subduction-related magmas:
691 petrological implications: Contributions to Mineralogy and Petrology, 138, 68–83.

692 Danyushevsky, L.V., McNeill, A.W., and Sobolev, A.V., 2002, Experimental and
693 petrological studies of melt inclusions in phenocrysts from mantle-derived magmas: an
694 overview of techniques, advantages and complications, Chemical Geology, 183, 5-24.

695 Davies, G.R., Cliff, R.A., Norry, M.J., and Gerlach, D.C., 1989, A combined chemical and
696 Pb-Sr-Nd isotope study of the Azores and Cape Verde hot-spots: the geodynamic
697 implications: Geological Society, London, Special Publications, 42, 231–255, doi:
698 10.1144/GSL.SP.1989.042.01.15.

699 Debret, B., Koga, K.T., Nicollet, C., Andreani, M., and Schwartz, S. (2013) F, Cl and S input
700 via serpentinite in subduction zones: implications for the nature of the fluid released at depth:
701 Terra Nova,, p. n/a–n/a, doi: 10.1111/ter.12074.

702 Dixon, J.E., Clague, D.A.and Stolper, E.M. (1991) Degassing History of Water, Sulfur, and
703 Carbon in Submarine Lavas from Kilauea Volcano, Hawaii (1991), The Journal of Geology,
704 99, 371-394

705 Dixon, J.E., and Stolper, E.M., 1995, An experimental study of water and carbon dioxide
706 solubilities in mid-ocean ridge basaltic liquids. Part II: applications to degassing: Journal of
707 Petrology, 36, 1633–1646.

708 Elliott, T., Blichert-Toft, J., Heumann, A., Koetsier, G., and Forjaz, V., 2007, The origin of
709 enriched mantle beneath São Miguel, Azores: Geochimica et Cosmochimica Acta, 71, 219–
710 240, doi: 10.1016/j.gca.2006.07.043.

711 Fortin, M.-A., Riddle, J., Desjardins-Langlais, Y., and Baker, D.R., 2015, The effect of water
712 on the sulfur concentration at sulfide saturation (SCSS) in natural melts, Geochimica et
713 Cosmochimica Acta, 160, 100–116, doi: 10.1016/j.gca.2015.03.022.

714 French, S.W., and Romanowicz, B., 2015, Broad plumes rooted at the base of the Earth's
715 mantle beneath major hotspots: Nature, 525, 95–99, doi: doi:10.1038/nature14876.

716 Gaetani, G.A., and Watson, E.B., 2000, Open system behavior of olivine-hosted melt
717 inclusions: Earth and Planetary Science Letters, 183, 27–41.

718 Gaetani, G.A., O'Leary, J.A., Shimizu, N., Bucholz, C.E., and Newville, M., 2012, Rapid
719 reequilibration of H2O and oxygen fugacity in olivine-hosted melt inclusions: Geology, v.
720 40, no. 10, p. 915–918, doi: 10.1130/G32992.1.

721 Gaetani, G.A., O'Leary, J.A., Koga, K.T., Hauri, E.H., Rose-Koga, E.F., and Monteleone,
722 B.D., 2014, Hydration of mantle olivine under variable water and oxygen fugacity
723 conditions: Contributions to Mineralogy and Petrology, 167, 965–14, doi: 10.1007/s00410-
724 014-0965-y.

725 Gale A., C. A. Dalton, C. H. Langmuir, Y. Su, and J.-G. Schilling (2013), The mean
726 composition of ocean ridge basalts, Geochem. Geophys. Geosyst., 14, 489–518,
727 doi:10.1029/2012GC004334.

728

729 Gao, S., Liu, X., Yuan, H., Hattendorf, B., Günther, D., Chen, L., and Hu, S., 2007,
730 Determination of Forty Two Major and Trace Elements in USGS and NIST SRM Glasses by
731 Laser Ablation-Inductively Coupled Plasma-Mass Spectrometry: Geostandards and
732 Geoanalytical Research, 26, 181–196, doi: 10.1111/j.1751-908X.2002.tb00886.x.

733 Ghiorso, M.S., 2015, MagmatSat app. Available through apple store.

734 Hauri, E. & Hart, S. R., 1993, Re-Os isotope systematics of HIMU and EMII oceanic island
735 basalts from the south Pacific Ocean. Earth Planetary Science Letters 114, 353–371.

736 Hanyu, T., Tatsumi, Y., and Kimura, J.-I., 2011, Constraints on the origin of the HIMU
737 reservoir from He–Ne–Ar isotope systematics: Earth and Planetary Science Letters, v. 307,
738 no. 3-4, p. 377–386, doi: 10.1016/j.epsl.2011.05.012.

739 Hart, S.R., and Gaetani, G.A., 2006, Mantle Pb paradoxes: the sulfide solution: Contributions
740 to Mineralogy and Petrology, 152, 295–308, doi: 10.1007/s00410-006-0108-1.

741 Hart, S.R., and Gaetani, G.A., 2016, Experimental determination of Pb partitioning between
742 sulfide melt and basalt melt as a function of P, T and X: Geochimica et Cosmochimica Acta,
743 doi: 10.1016/j.gca.2016.01.030.

744 Hawkesworth, C.J., Norry, M.J., Roddick, J.C., and Vollmer, R., 1979, 143Nd/144Nd and
745 87Sr/86Sr ratios from the Azores and their significance in LIL-element enriched mantle:
746 Nature, 280, 28–31, doi: 10.1038/280028a0.

747 Helo, C., Longpré, M.-A., Shimizu, N., Clague, D.A., and Stix, J., 2011, Explosive eruptions
748 at mid-ocean ridges driven by CO_2-rich magmas: Nature Geoscience, 4, 260–263, doi:
749 10.1038/ngeo1104.

750 Hofmann, A.W., 1997, Mantle geochemistry: the message from oceanic volcanism: Nature, v.
751 385, no. 6613, p. 219–229.

752 Jackson M.G., Koga K.T., Price A., Konter J.G., Koppers A.A.P., Finlayson V.A., Konrad K.,
753 Hauri E.H., Kylander-Clark A., Kelley K.A., Kendrick M.A., 2015, Deeply-dredged
754 Submarine HIMU Glasses from the Tuvalu Islands, Polynesia: Implications for Volatile
755 Budgets of Recycled Oceanic Crust, Paper #2015GC005966R, in press Geochemistry
756 Geophysics Geosystems.

757 Jochum, K.P., Stoll, B., Herwig, K., Willbold, M., Hofmann, A.W., Amini, M., Aarburg, S.,
758 Abouchami, W., Hellebrand, E., Mocek, B., Raczek, I., Stracke, A., Alard, O., Bouman, C.,
759 et al., 2006, MPI-DING reference glasses for in situ microanalysis: New reference values for
760 element concentrations and isotope ratios: Geochemistry Geophysics Geosystems, 7, doi:
761 10.1029/2005GC001060.

762 Johnson, C. L., J. R. Wijbrans, C. G. Constable, J. Gee, H. Staudigel, L. Tauxe, V.-H. Forjaz
763 and M. Salgueiro, 1998, "40Ar/39Ar ages and paleomagnetism of Sao Miguel lavas,Azores."
764 Earth and Planetary Science Letters 160: 637-649.

765 Kelley, K.A., Kingsley, R., and Schilling, J.-G., 2013, Composition of plume-influenced
766 mid-ocean ridge lavas and glasses from the Mid-Atlantic Ridge, East Pacific Rise, Galápagos
767 Spreading Center, and Gulf of Aden: Geochemistry Geophysics Geosystems, 14, 223–242,
768 doi: 10.1002/ggge.20049.

769 Kendrick, M.A. Scambelluri, M., Honda, M., and Phillips, D., 2011, High abundances of
770 noble gas and chlorine delivered to the mantle by serpentinite subduction : Nature
771 Geoscience : Nature Publishing Group: Nature Geoscience, v. 4, p. 807–812, doi:
772 10.1038/NGEO1270.

773 Kendrick, M.A., Woodhead, J.D., and Kamenetsky, V.S., 2012, Tracking halogens through
774 the subduction cycle: Geology, v. 40, no. 12, p. 1075–1078, doi: 10.1130/G33265.1.

775 Kendrick, M.A., Jackson, M.G., Kent, A.J.R., Hauri, E.H., Wallace, P.J., and Woodhead, J.,
776 2014, Contrasting behaviours of CO_2, S, H_2O and halogens (F, Cl, Br, and I) in enriched-
777 mantle melts from Pitcairn and Society seamounts: Chemical Geology, 370, 69–81, doi:
778 10.1016/j.chemgeo.2014.01.019.

779 Kiseeva, E.S., and Wood, B.J., 2015, The effects of composition and temperature on
780 chalcophile and lithophile element partitioning into magmatic sulphides: Earth and Planetary
781 Science Letters.

782 Koleszar, A.M., Saal, A.E., Hauri, E.H., Nagle, A.N., Liang, Y., and Kurz, M.D., 2009, The
783 volatile contents of the Galapagos plume; evidence for H2O and F open system behavior in
784 melt inclusions: Earth and Planetary Science Letters, 287, 442–452, doi:
785 10.1016/j.epsl.2009.08.029.

786 Kurz M.D., 1993, Mantle heterogeneity beneath ocean islands: some inferences from :
787 isotopes. Philos. Trans. R. Soc. London 342, 91-103.

788 Lassiter, J., Hauri, E.H., Nikogosian, I., and Barsczus, H., 2002, Chlorine–potassium
789 variations in melt inclusions from Raivavae and Rapa, Austral Islands: constraints on
790 chlorine recycling in the mantle and evidence for brine-induced melting of oceanic crust:
791 Earth and Planetary Science Letters, 202, 525–540.

792 Le Bas, M.J.L., Lemaitre, R.W.L., Streckeisen, A., Zanettin, B., and Rocks, 1986, A
793 Chemical Classification of Volcanic Rocks Based on the Total Alkali-Silica Diagram,
794 Journal of Petrology, 27, 745–750.

795 Le Voyer, M., Rose-Koga, E.F., Laubier, M., and Schiano, P., 2008, Petrogenesis of arc lavas
796 from the Rucu Pichincha and Pan de Azucar volcanoes (Ecuadorian arc): Major, trace
797 element, and boron isotope evidences from olivine-hosted melt inclusions: Geochemistry
798 Geophysics Geosystems, 9, doi: 10.1029/2008GC002173.

799 Le Voyer, M., Rose-Koga, E.F., Shimizu, N., Grove, T.L., and Schiano, P., 2010, Two
800 Contrasting H2O-rich Components in Primary Melt Inclusions from Mount Shasta: Journal of
801 Petrology, 51, 1571–1595, doi: 10.1093/petrology/egq030.

802 Le Voyer, M., E. Cottrell, K. A. Kelley, M. Brounce, and E. H. Hauri, 2015, The effect of
803 primary versus secondary processes on the volatile content of MORB glasses: An example
804 from the equatorial Mid-Atlantic Ridge (5°N–3°S), J. Geophys. Res. Solid Earth, 120, 125–
805 144, doi:10.1002/2014JB011160.

806 Li and Naldrett, 1993 Sulfide capacity of magma; a quantitative model and its application to
807 the formation of sulfide ores at Sudbury, Ontario, Economic Geology, 88, 1253-1260

808 Li and Ripley, 2009, Sulfur Contents at Sulfide-Liquid or Anhydrite Saturation in Silicate
809 Melts: Empirical Equations and Example Applications, Economic Geology, 104, 405-412

810 Liu, Y., Samaha, N.-T., and Baker, D.R., 2007, Sulfur concentration at sulfide saturation
811 (SCSS) in magmatic silicate melts, Geochimica et Cosmochimica Acta, 71, 1783–1799, doi:
812 10.1016/j.gca.2007.01.004.

813 Madureira, P., Moreira, M., Mata, J., and Nunes, J.C., 2014, Helium isotope systematics in
814 the vicinity of the Azores triple junction: Constraints on the Azores geodynamics, Chemical
815 Geology, 372, 62–71.

816 Métrich, N., Zanon, V., Créon, L., Hildenbrand, A., Moreira, M., and Marques, F.O., 2014, Is

817 the “Azores Hotspot” a Wetspot? Insights from the Geochemistry of Fluid and Melt
818 Inclusions in Olivine of Pico Basalts, Journal of Petrology, 55, 377–393.

819 Michael, P.J., 1988, The concentration, behavior and storage of H_2O in the suboceanic upper
820 mantle, Implications for mantle metasomatism, Geochimica et Cosmochimica Acta, 52, 555-
821 566.

822 Michael, P.J., and Cornell, W.C., 1998, Influence of spreading rate and magma supply on
823 crystallization and assimilation beneath mid-ocean ridges: Evidence from chlorine and major
824 element chemistry of mid-ocean ridge basalts, Journal of Geophysical Research, 103, 18325–
825 18–356.

826 Millet, M.-A., R. Doucelance, J. A. Baker and P. Schiano (2009). "Reconsidering the origins
827 of isotopic variations in Ocean Island Basalts: Insights from fine-scale study of São Jorge
828 Island, Azores archipelago." Chemical Geology 265: 289-302.

829 Moore, R.B., 1990, Volcanic geology and eruption frequency, São Miguel, Azores, Bulletin
830 of Volcanology, 52, 602–614.

831 Moreira, M., Doucelance, R., Kurz, M., and Dupre, B., 1999, Helium and lead isotope
832 geochemistry of the Azores Archipelago: Earth and Planetary Science Letters, 169, 189–205.

833 Moreira, M., Kanzari, A. and Madureira, P., 2012, Helium and neon isotopes in São Miguel
834 island basalts, Azores Archipelago: New constraints on the “low 3He” hotspot origin,
835 Chemical Geology, 322-323, 91–98.

836 O’Neill HS, Mavrogenes JA (2002) The sulfide capacity and the sulfur content at sulfide
837 saturation of silicate melts at 1400 °C and 1 bar, Journal of Petrology 43:1049-1087

838 Patten, C., Barnes, S.J., Mathez, E.A., and Jenner, F.E., 2013, Partition coefficients of
839 chalcophile elements between sulfide and silicate melts and the early crystallization history
840 of sulfide liquid: LA-ICP-MS analysis of MORB sulfide droplets, Chemical Geology, 358,
841 170–188.

842 Peacock, S.A., 1990, Fluid processes in subduction zones: Science, 248, 329–337.

843 Rose-Koga E.F., Shimizu N., Devidal J-L, Koga K.T., Le Voyer M., 2008, Investigation of F,
844 S, and Cl Standards by ion Probe and Electron Microprobe, Eos Trans. AGU, 89(53), Fall
845 Meet. Suppl., Abstract V31B-2145.

846 Rose-Koga, E.F., Koga, K., Schiano, P., and Le Voyer, M., 2012, Mantle source
847 heterogeneity for South Tyrrhenian magmas revealed by Pb isotopes and halogen contents of
848 olivine-hosted melt inclusions, Chemical Geology, 334, 266–279.

849 Rose-Koga, E.F., Koga, K.T., Hamada, M., Hélouis, T., Whitehouse, M.J., and Shimizu, N.,
850 2014, Volatile (F and Cl) concentrations in Iwate olivine-hosted melt inclusions indicating
851 low-temperature subduction, Earth, Planets and Space, 66, 81, doi: 10.1029/2000GL012558.

852 Saal, A.E., Hart, S.R., Shimizu, N., Hauri, E.H., Layne, G., and Eiler, J., 2005, Pb isotopic
853 variability in melt inclusions from the EMI–EMII–HIMU mantle end-members and the role
854 of the oceanic lithosphere, Earth and Planetary Science Letters, 240, 605–620, doi:
855 10.1016/j.epsl.2005.10.002.

856 Salters, V.J.M., and Stracke, A., 2004, Composition of the depleted mantle, Geochemistry
857 Geophysics Geosystems, 5, doi: 10.1029/2003GC000597.

858 Schilling, J.-G., Bergeron, M.B., Evans, R., 1980. Halogens in the mantle beneath the North
859 Atlantic. Philos. Trans. R. Soc. London 297, 147-178.

Seyfried, W.E., Jr, and Ding, K., 1995, The hydrothermal chemistry of fluoride in seawater: Geochimica et Cosmochimica Acta, 59, 1063–1071, doi: 10.1016/0016-7037(95)00023-S.

Shaw, A.M., Hauri, E.H., Fischer, T.P., Hilton, D.R., and Kelley, K.A., 2008, Hydrogen isotopes in Mariana arc melt inclusions: Implications for subduction dehydration and the deep-Earth water cycle: Earth and Planetary Science Letters, 275, 138–145, doi: 10.1016/j.epsl.2008.08.015.

Shaw, A.M., Behn, M.D., Humphris, S.E., Sohn, R.A., and Gregg, P.M., 2010, Deep pooling of low degree melts and volatile fluxes at the 85°E segment of the Gakkel Ridge: Evidence from olivine-hosted melt inclusions and glasses, Earth and Planetary Science Letters, 289, 311–322, doi: 10.1016/j.epsl.2009.11.018.

Shimizu, K., Saal, A.E., Myers, C.E., Nagle, A.N., Hauri, E.H., Forsyth, D.W., Kamenetsky, V.S., and Niu, Y., 2016, Two-component mantle melting-mixing model for the generation of mid-ocean ridge basalts: Implications for the volatile content of the Pacific upper mantle, Geochimica et Cosmochimica Acta, 176, 44–80, doi: 10.1016/j.gca.2015.10.033.

Smith, J.V., 1981, Halogen and phosphorus storage in the Earth, Nature, 289, 762–765, doi: 10.1038/289762a0.

Sobolev, A.V., and Chaussidon, M., 1996, H2O concentrations in primary melts from supra-subduction zones and mid-ocean ridges: Implications for H2O storage and recycling in the mantle, Earth and Planetary Science Letters, 137, 45–55.

Spilliaert, N., Métrich, N., and Allard, P., 2006, S–Cl–F degassing pattern of water-rich alkali basalt: Modelling and relationship with eruption styles on Mount Etna volcano, Earth and Planetary Science Letters, 248, 772–786, doi: 10.1016/j.epsl.2006.06.031.

Stefano, C.J., Mukasa, S.B., Andronikov, A., and Leeman, W.P., 2011, Water and other volatile systematics of olivine-hosted melt inclusions from the Yellowstone hotspot track, Contributions to Mineralogy and Petrology, 161, 615–633, doi: 10.1007/s00410-010-0553-8.Sobolev and Chaussidon, 1996

Straub, S.M., and Layne, G.D. (2003) The systematics of chlorine, fluorine, and water in Izu arc front volcanic rocks: Implications for volatile recycling in subduction zones: Geochimica et Cosmochimica Acta, 67, 4179–4203, doi: 10.1016/S0016-7037(03)00307-7.

Sun, S.S., and McDonough, W.F., 1989, Chemical and isotopic systematics of oceanic basalts: implications for mantle composition and processes: Geological Society, London, Special Publications, 42, 313–345, doi: 10.1144/GSL.SP.1989.042.01.19.

Thordarson, T., Self, S., Oskarsson, N., and Hulsebosch, T., 1996, Sulfur, chlorine, and fluorine degassing and atmospheric loading by the 1783-1784 AD Laki (Skaftar Fires) eruption in Iceland: Bulletin of Volcanology, 58, 205–225, doi: 10.1007/s004450050136.

Toplis, M.J., 2005, The thermodynamics of iron and magnesium partitioning between olivine and liquid: criteria for assessing and predicting equilibrium in natural and experimental systems, Contributions to Mineralogy and Petrology, 149, 22–39, doi: 10.1007/s00410-004-0629-4.

Turner, S., Hawkesworth, C., Rogers, N., and King, P., 1997, U-Th isotope disequilibria and ocean island basalt generation in the Azores: Chemical Geology, 139, 145–164.

Van den Bleeken, G., and Koga, K.T. (2015) Experimentally determined distribution of fluorine and chlorine upon hydrous slab melting, and implications for F–Cl cycling through subduction zones: Geochimica et Cosmochimica Acta, 171, 353–373.

Van Keken, P.E., 2002, High-resolution models of subduction zones: Implications for mineral dehydration reactions and the transport of water into the deep mantle: Geochemistry Geophysics Geosystems, 3, doi: 10.1029/2001GC000256.

Vlastélic, I., Gannoun, A., Di Muro, A., and Gurioli, L., 2016, Origin and fate of sulfide liquids in hotspot volcanism (La Réunion): Pb isotope constraints from residual Fe-Cu oxides, Geochimica et Cosmochimica Acta, doi: http://dx.doi.org/10.1016/j.gca.2016.08.036.

Vogt, P.R., and Jung, W.Y., 2004, The Terceira Rift as hyper-slow, hotspot-dominated oblique spreading axis: A comparison with other slow-spreading plate boundaries: Earth and Planetary Science Letters, 218, 77–90.

Wallace, P., and Carmichael, I.S.E., 1992, Sulfur in basaltic magmas: Geochimica et Cosmochimica Acta, 56, 1863–1874, doi: 10.1016/0016-7037(92)90316-B.

Wanless, V.D., and Shaw, A.M., 2012, Lower crustal crystallization and melt evolution at mid-ocean ridges: Nature Geoscience, 5, 651–655, doi: 10.1038/ngeo1552.

Wanless, V.D., Shaw, A.M., Behn, M.D., Soule, S.A., Escartin, J., and Hamelin, C., 2015, Magmatic plumbing at Lucky Strike volcano based on olivine-hosted melt inclusion compositions, Geochem. Geophys. Geosyst., 16, 126–147, doi:10.1002/2014GC005517.

Warren, J.M., and Shirey, S.B., 2012, Lead and osmium isotopic constraints on the oceanic mantle from single abyssal peridotite sulfides: Earth and Planetary Science Letters, v. 359-360, p. 279–293, doi: 10.1016/j.epsl.2012.09.055.

White, W.M., Tapia, M.D.M., and Schilling, J.-G., 1979, The petrology and geochemistry of the Azores Islands: Contributions to Mineralogy and Petrology, 69, 201–213, doi: 10.1007/BF00372322.

White, W.M., 2015, Isotopes, DUPAL, LLSVPs, and Anekantavada: Chemical Geology, 419, 10–28, doi: 10.1016/j.chemgeo.2015.09.026.

Widom, E., and Shirey, S.B., 1996, Os isotope systematics in the Azores: implications for mantle plume sources: Earth and Planetary Science Letters, 142, 451–465.

Widom, E., Carlson, R., Gill, J., and Schmincke, H.U., 1997, Th-Sr-Nd-Pb isotope and trace element evidence for the origin of the Sao Miguel, Azores, enriched mantle source: Chemical Geology, 140, 49–68.

Widom, E., 2002, Earth science: Ancient mantle in a modern plume: Nature a-z index, 420, 281–282.

Widom, E., and Farquhar, J., 2003, Oxygen isotope signatures in olivines from Sao Miguel (Azores) basalts: implications for crustal and mantle processes: Chemical Geology, 193, 237–255.

Witham, F., Blundy, J., Kohn, S.C., Lesne, P., Dixon, J., Churakov, S.V., and Botcharnikov, R., 2012, SolEx: A model for mixed COHSCl-volatile solubilities and exsolved gas compositions in basalt, Computers & Geosciences, 45, 87–97, doi: 10.1016/j.cageo.2011.09.021.

Wood, B.J., and Kiseeva, E.S., 2015, Trace element partitioning into sulfide: How lithophile elements become chalcophile and vice versa: American Mineralogist, 100, 2371–2379, doi: 10.2138/am-2015-5358CCBYNCND.

Woodhead, J.D., and Devey, C.W., 1993, Geochemistry of the Pitcairn seamounts, I: source character and temporal trends: Earth and Planetary Science Letters, 116, 81-99.

947 Workman, R.K., Hauri, E.H., Hart, S.R., Wang, J., and Blusztajn, J., 2006, Volatile and trace
948 elements in basaltic glasses from Samoa: Implications for water distribution in the mantle:
949 Earth and Planetary Science Letters, 241, 932–951, doi: 10.1016/j.epsl.2005.10.028.

950 Wu, J., and Koga, K.T., 2013, Fluorine partitioning between hydrous minerals and aqueous
951 fluid at 1GPa and 770–947°C: A new constraint on slab flux: Geochimica et Cosmochimica
952 Acta, 119, 77–92.

953 Zindler, A., Hart, S.R., 1986. Chemical geodynamics. Annu. Rev. Earth Planet. Sci., 14, 493–
954 571, doi:10.1146/annurev.ea.14.050186.002425

Figure captions

Fig. 1: Simplified map of the Azores archipelago. The names of the islands are abbreviated as follows: Fl stands for Flores, C for Corvo, G for Graciosa, F for Faial, P for Pico, SJ for Sao Jorge, T for Terceira, SMi for Sao Miguel and SMa for Santa Maria. Sample locations are on Sao Miguel Island (37.7667° N, 25.4667° W, the eastern most island of the Azores archipelago). São Miguel is a 50 km long island composed of 5 volcanic complexes: Sete Cidades, Picos, Fogo, Furnas, and Nordeste. Three volcanoes are active (Sete Cidades, Agua de Pau, and Furnas) and the older Nordeste complex is extinct. The six samples we studied came from Picos, Fogo, and Nordeste.

Fig. 2: Le Bas classification of Azores whole rocks and melt inclusions. Total alkali (Na_2O+K_2O) is plotted as a function of SiO_2 in wt% (Le Bas et al., 1986). Azores whole rocks vary from picrobasalts to trachyte, and the melt inclusions (bigger symbols) represent less evolved magmas, mostly in the fields of basalt and tephrite basanite with some extension towards trachy-basalt to basaltic trachy-andesite.

Fig. 3: (a) Trace element patterns of São Miguel melt inclusions (thin black lines) of this study, of Pico melt inclusions (thin gray lines), and of an average N-MORB composition (dashed line; normalization to primitive mantle and N-MORB composition are from Sun and McDonough, 1989). Previously reported whole rock data are shown as the shaded area; all whole rock data was filtered for São Miguel basalts (SiO_2 < 53 wt. %; White at al., 1979; Davies et al., 1989; Turner et al., 1997; Beier et al., 2006, 2007; Madureira et al., 2014). The lack of pronounced kinks at Sr and Eu discards notable addition or subtraction of plagioclase. (b) REE patterns of São Miguel melt inclusions (thin solid lines) and whole rocks (shaded area); references are as in (a).

Fig. 4: $^{207}Pb/^{206}Pb$ versus $^{208}Pb/^{206}Pb$ for São Miguel melt inclusions (ellipse errors represent 2σ standard error of the mean) and the corresponding whole rock measured at LMV (larger symbols, errors are largely within the size of the symbols). Pb-isotope compositions of the whole rocks and 19 melt inclusions (not counting duplicates) are represented: samples ACO95-03, ACO95-56, ACO95-62, and ACO95-68 include whole rock measurements and melt inclusions; whole rock Pb isotopes of 2000-4 and 2000-9 were not measured. The 2σ ellipsoid errors for repeat measurements of standard glasses with 19 ppm (GOR132G standard; Jochum et al., 2006) and 2 ppm Pb (R124, Reunion island glass) are represented at top-left to indicate the external reproducibility. Melt inclusions plot generally in the vicinity of their whole rock, extending in some cases (ACO95-62 and ACO95-56) the range of Pb isotope compositions of the lava, indicating that some melt inclusions appear to show heterogeneity of parental magmas.

Fig. 5: Insert: at a given $^{206}Pb/^{204}Pb$, São Miguel whole rocks (red open circles in the pink area) have higher $^{208}Pb/^{204}Pb$ than Central Group rocks (shaded grey area). São Miguel melt inclusions were chosen from whole rocks that best represent the extreme composition of the "Nordeste component". Main figure: $^{207}Pb/^{206}Pb$ versus $^{208}Pb/^{206}Pb$, with São Miguel melt inclusions (filled red circles, this study) compared to melt inclusions, glasses, and whole rocks from islands representing different mantle endmembers. Data represented here are not extensive (filtered for SiO_2 < 53 wt. %) and do not represent all the published data. Melt inclusions are filled symbols, and open symbols are whole rocks or glasses. Symbol shapes are specific to each locality. Data sources are: São Miguel whole rocks (Davies et al., 1989; Turner et al., 1997; Widom et al., 1997; Moreira et al., 1999; Elliott et al., 2007; Beier et al.,

2007); Mangaia (HIMU) melt inclusions (Cabral et al., 2014); Pitcairn (EMI) glasses (Woodhead and Devey, 1993); MAR whole rocks and glasses (Agranier et al., 2005; Kelley et al., 2013); Samoa (EMII) glasses (Workman et al., 2006); and Tahaa (EMII) melt inclusions (Saal et al., 2005). Whole rock and melt inclusions of São Miguel mainly overlap. The 2σ ellipsoid errors for repeat measurements of standard glasses with 19 ppm (GOR132G standard; Jochum et al., 2006) and 2 ppm Pb (R124, Reunion island glass) are represented next to the legend to indicate the external reproducibility.

Fig. 6: Cl concentrations (ppm) as a function of F concentrations (ppm) in São Miguel melt inclusions (this study) and in Pico island melt inclusions (Métrich et al., 2014). Our data are compared to measurements of melt inclusions (filled symbols) and glasses (open symbols) from localities representing different mantle endmembers: Yellowstone melt inclusions (Stefano et al., 2011), Cook Austral melt inclusions (Lassiter et al., 2002), MORB melt inclusions (Shaw et al., 2010, Wanless and Shaw, 2012) and glasses (Le Voyer et al., 2015), Pitcairn glasses (Kendrick et al., 2014), Samoa melt inclusions and glasses (Workman et al., 2006), and Mangaia melt inclusions (Cabral et al., 2014). Azores melt inclusions are enriched in F and Cl by a factor of 10 compared to MORB glasses. F and Cl concentrations in melt inclusions from Azores and Mangaia mainly overlap and are relatively clustered. Azores melt inclusions are the lowest among OIBs.

Fig. 7: F/Nd as a function of Cl/K_2O in São Miguel melt inclusions and other mantle endmember localities (symbols and references as in Fig. 7). Tuvalu glass data (brown open diamonds) are also plotted since they might represent "real HIMU" volatile element compositions (Jackson et al., 2015). MORB and Samoan data that were suspected of assimilation of seawater contaminated material are represented by smaller, lighter symbols when $Cl/K_2O>0.05$ (Michael and Cornell, 1998). The $Cl/K_2O>0.05$ 'cut-off' discards much of the Cook Austral data (Lassiter et al., 2002) since they suffered from assimilation of seawater related components. There is a positive correlation (outlined by the shaded gray area) between F/Nd and Cl/K_2O from melt inclusions or glasses from OIBs representing mantle endmembers (Samoa EMII, Pitcairn EMI, Mangaia HIMU), and Azores melt inclusions from Pico (Métrich et al., 2014) and São Miguel (this study) plot along this correlation. The relatively tight domain of variation for São Miguel melt inclusions allows us to propose characteristic values of Cl/K_2O (0.035±0.011) and F/Nd (23.1±3.4) for the São Miguel parental magma.

Fig. 8: $^{207}Pb/^{206}Pb$ (red filled circles, red scale at left) and FeO concentrations (blue crosses, blue scale at right) plotted against S concentrations in ppm for São Miguel melt inclusions. São Miguel melt inclusions are at sulfide saturation, which explains the relationship between S and FeO (the solubility of S increases with increasing FeO content at sulfide saturation; e.g. Li and Naldrett, 1993; O'Neill and Mavrogenes, 2002). Curves represent model results of mixing between sulfide and basaltic melts for two contrasting Kd^{Pb} values (following Hart and Gaetani, 2016) of 140 (top curve) and 30 (bottom curve). The best fit to our data is represented by the center curve ($Kd^{Pb}=70$). The sulfide melt is a FeS melt (S =360000ppm; $^{207}Pb/^{206}Pb$ =0.857) and the basaltic melt corresponds to Pb=2ppm and $^{207}Pb/^{206}Pb$ =0.780, with S=500ppm (the lowest S concentrations measured in our melt inclusions). Tick marks along the curves are 0.06% increments of the sulfide melt mixing proportion. Less than 0.4% of sulfide is needed to account for the positive correlation of Pb-isotopes and S contents observed in our melt inclusions. Pb concentration in the sulfide must be high, between 60 and 280 ppm, indicating the sulfide is of shallow origin (Hart and Gaetani, 2016).

Fig. 9: S concentration measured in São Miguel melt inclusions as a function of Sulfur Concentration at Sulfide Saturation. SCSS is calculated following Fortin et al. (2015). For melt inclusions not analysed for H_2O content, we assumed H_2O=1552 ppm, the maximum measured H_2O of this study; this value most likely represents a minimum value because they melt inclusions are already partly degassed (see section 5.2.1 for details). Temperature was set at 1200ºC (homogenization temperature) and we conservatively chose the pressure value to be 0.012 MPa, the lowest given by our São Miguel melt inclusions (MagmaSat calculation). Using our maximum pressure value slightly shifts points to the left, but the two undersaturated melt inclusions remain undersaturated. Error bars represent 20% relative uncertainty on the sulfur measurements. The area between the thin dotted lines is the uncertainty band representing a variation of ±50% around an ideal value (see Fig. 6b of Fortin et al., 2015; assessed by the relative difference between modelled S and measured S concentrations for natural samples with less than 2000 ppm S). All São Miguel melt inclusions are at S saturation (red filled symbols) except for two S-undersaturated melt inclusions (ACO95-62i, its replicate, and 9-4-00; 3 white circles). One representative Pico melt inclusion (yellow filled circle) is reported for comparison; it is also at S saturation.

Fig. 10: F/Nd as a function of $^{207}Pb/^{206}Pb$ for São Miguel melt inclusions and mantle endmembers HIMU, EMI, EMII, and DMM. References and symbols are as in Figure 7; E-MORB glass/melt inclusion data are from Gale et al., 2013; Shimizu et al., 2016. The glasses and melt inclusions from the mantle endmembers define a negative trend between F/Nd and $^{207}Pb/^{206}Pb$, and São Miguel melt inclusions fall on this correlation. F/Nd is therefore a reliable tracer of source when comparing OIBs. F/Nd of São Miguel melt inclusions (23.1±3.4) is similar within error to the value of the canonical ratio 21±4 (Workman et al., 2006).

Figure1

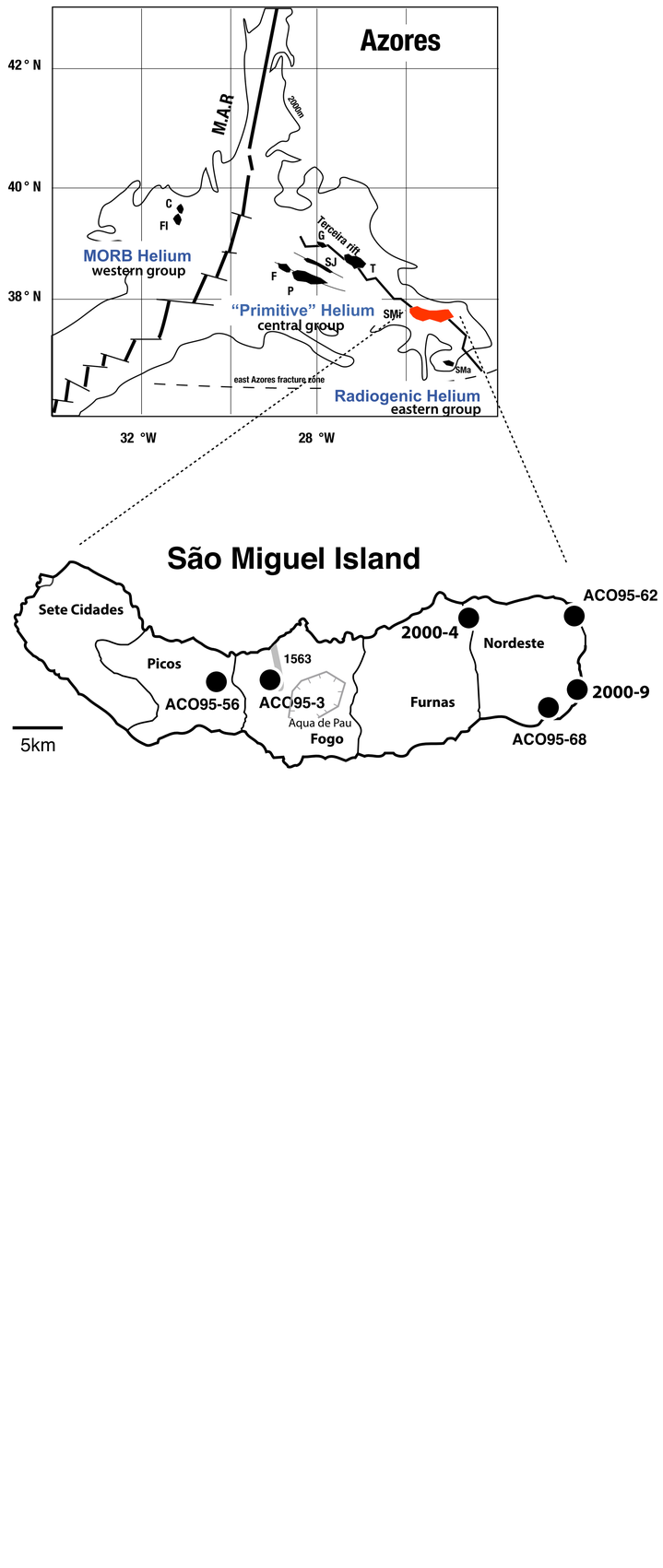
Azores
42 ° N
40 ° N
38 ° N
32 °W
28 °W
M.A.R
200m
C
FI
Terceira rift
G
SJ
T
F
P
MORB Helium
western group
"Primitive" Helium
central group
SMF
SMa
east Azores fracture zone
Radiogenic Helium
eastern group
São Miguel Island
Sete Cidades
Picos
ACO95-56
1563
ACO95-3
Água de Pau
Fogo
Furnas
2000-4
Nordeste
ACO95-62
2000-9
ACO95-68
5km

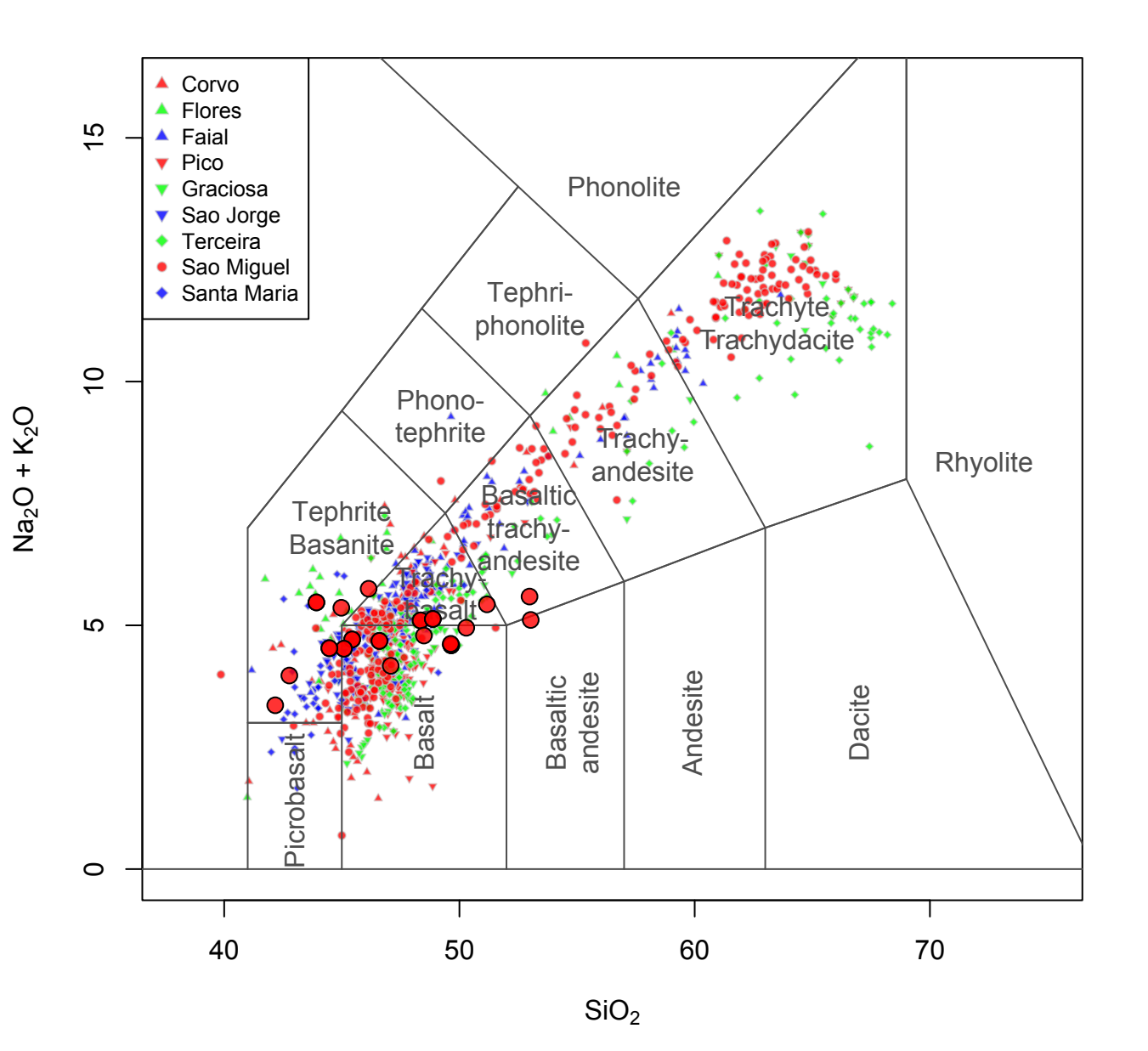
Corvo
Flores
Faial
Pico
Graciosa
Sao Jorge
Terceira
Sao Miguel
Santa Maria
Phonolite
Tephri-
phonolite
Phono-
tephrite
Tephrite
Basanite
Basaltic
trachy-
andesite
Trachy-
basalt
Trachyte
Trachydacite
Trachy-
andesite
Rhyolite
Picrobasalt
Basalt
Basaltic
andesite
Andesite
Dacite
0
5
10
15
40
50
60
70
$Na_2O + K_2O$
SiO_2

Figure3a

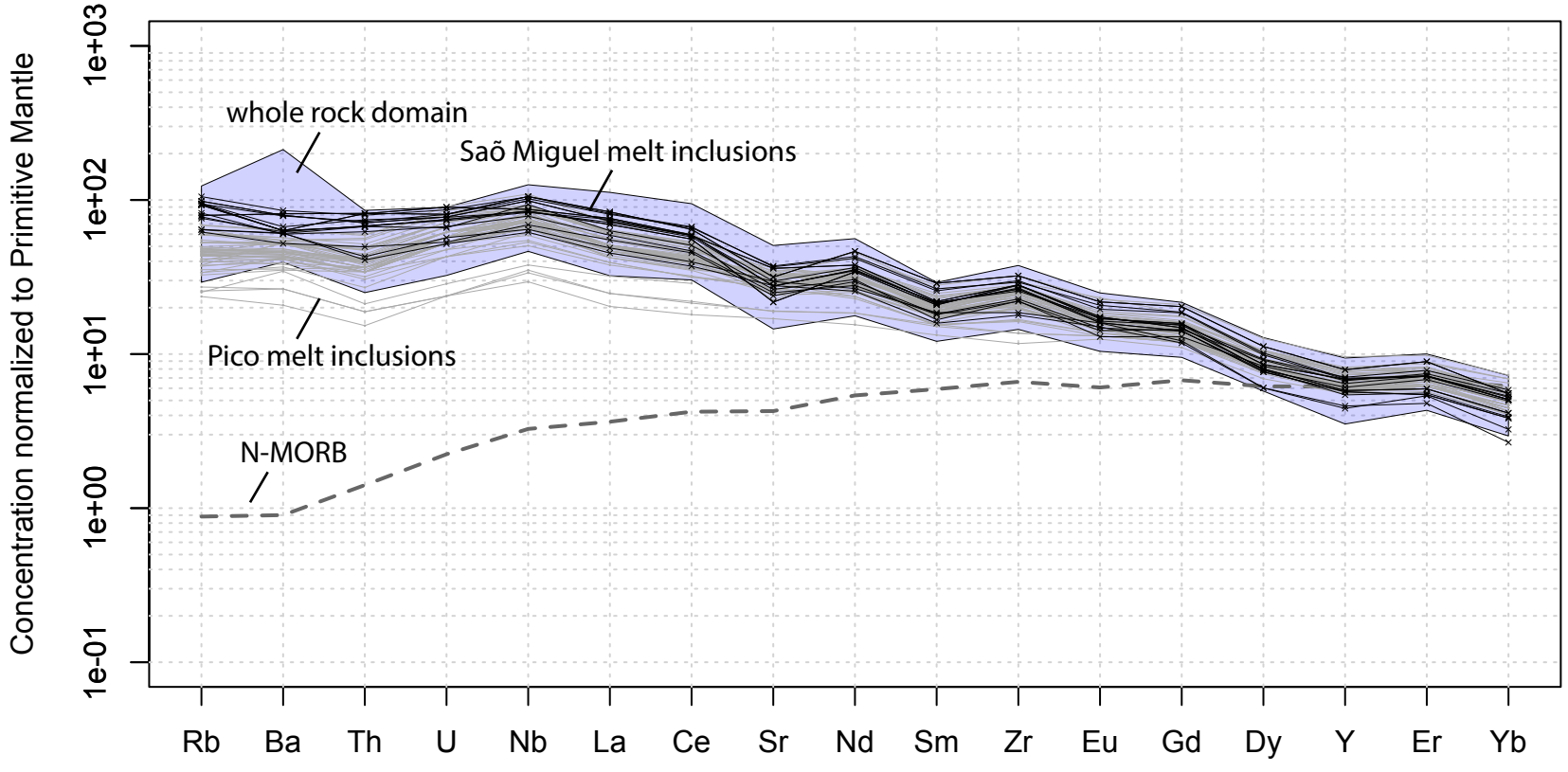
Concentration normalized to Primitive Mantle
1e-01
1e+00
1e+01
1e+02
1e+03
whole rock domain
Saõ Miguel melt inclusions
Pico melt inclusions
N-MORB
Rb
Ba
Th
U
Nb
La
Ce
Sr
Nd
Sm
Zr
Eu
Gd
Dy
Y
Er
Yb

Figure3b

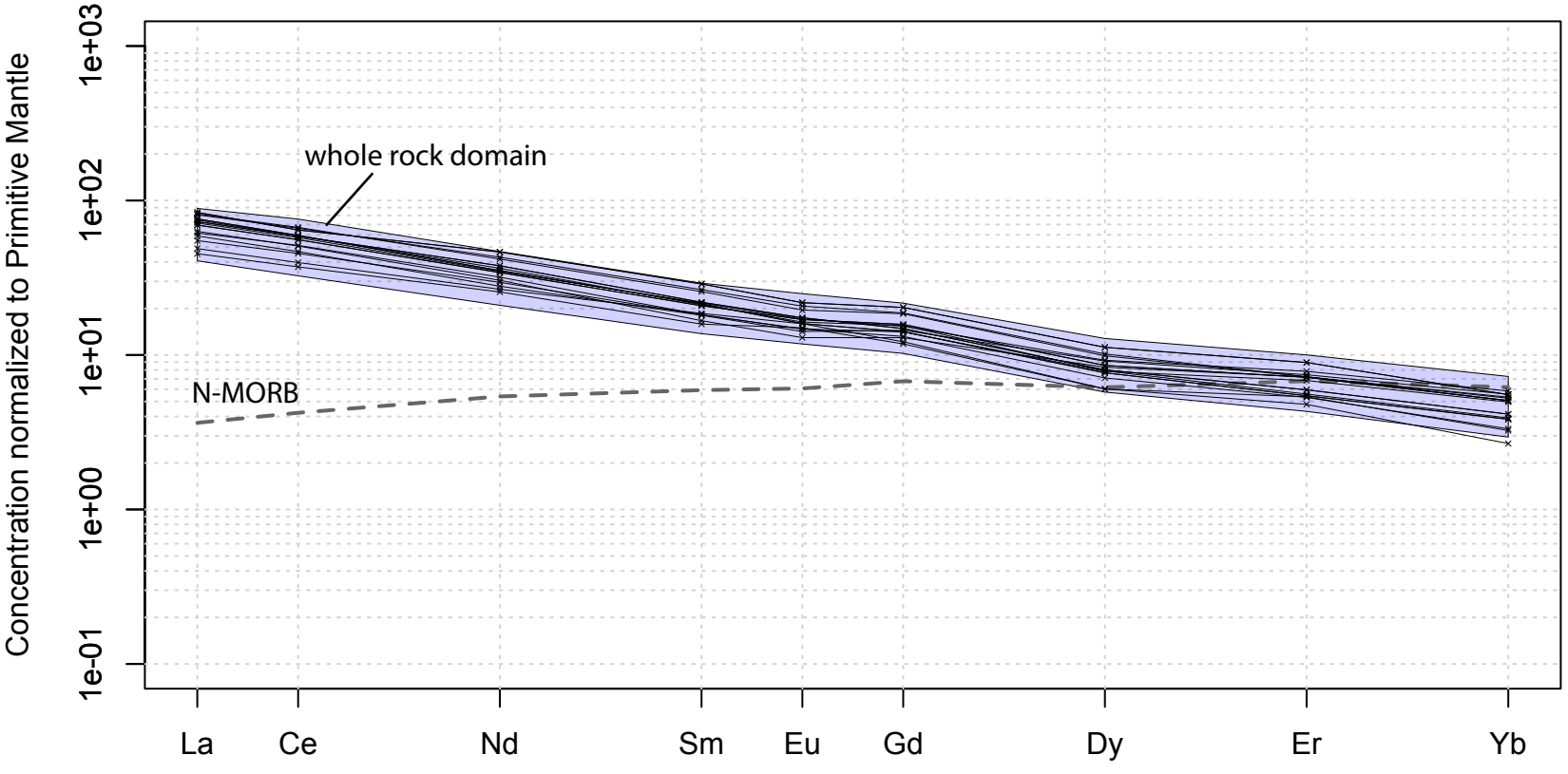
Concentration normalized to Primitive Mantle
1e+03
1e+02
1e+01
1e+00
1e-01
whole rock domain
N-MORB
La
Ce
Nd
Sm
Eu
Gd
Dy
Er
Yb

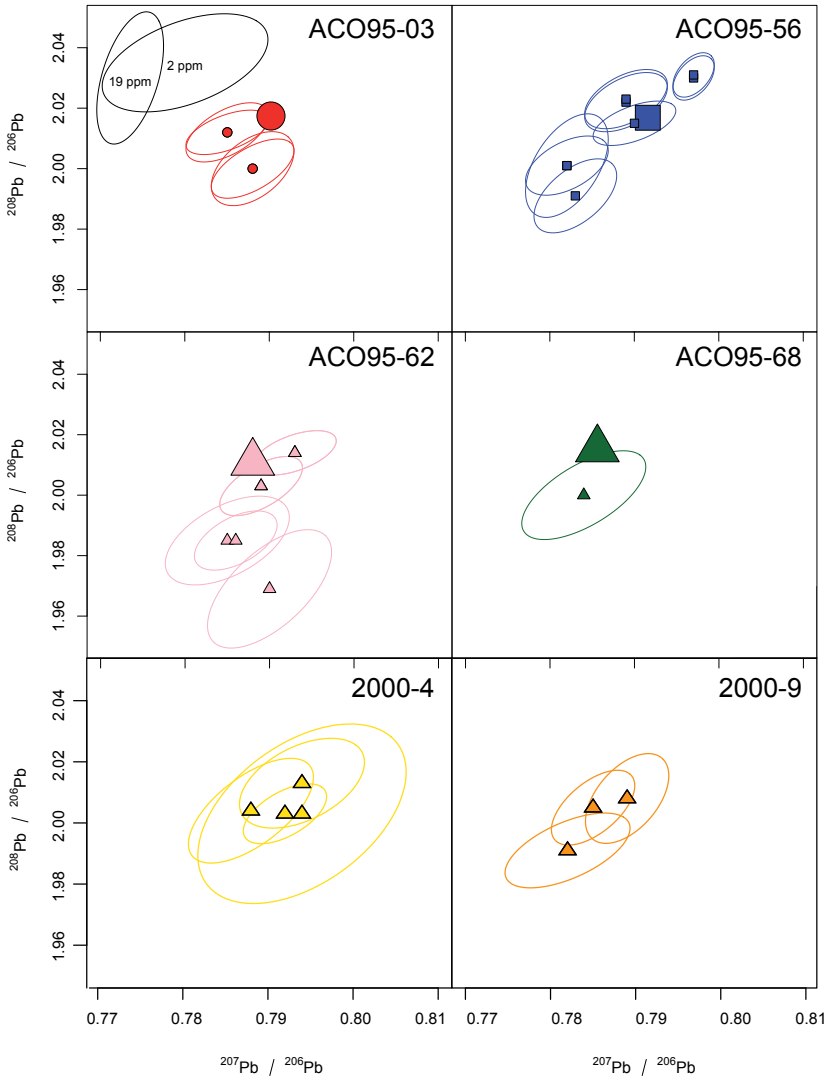
ACO95-03
19 ppm
2 ppm
ACO95-56
ACO95-62
ACO95-68
2000-4
2000-9
208Pb / 206Pb
207Pb / 206Pb
1.96
1.98
2.00
2.02
2.04
0.77
0.78
0.79
0.80
0.81

Figure5

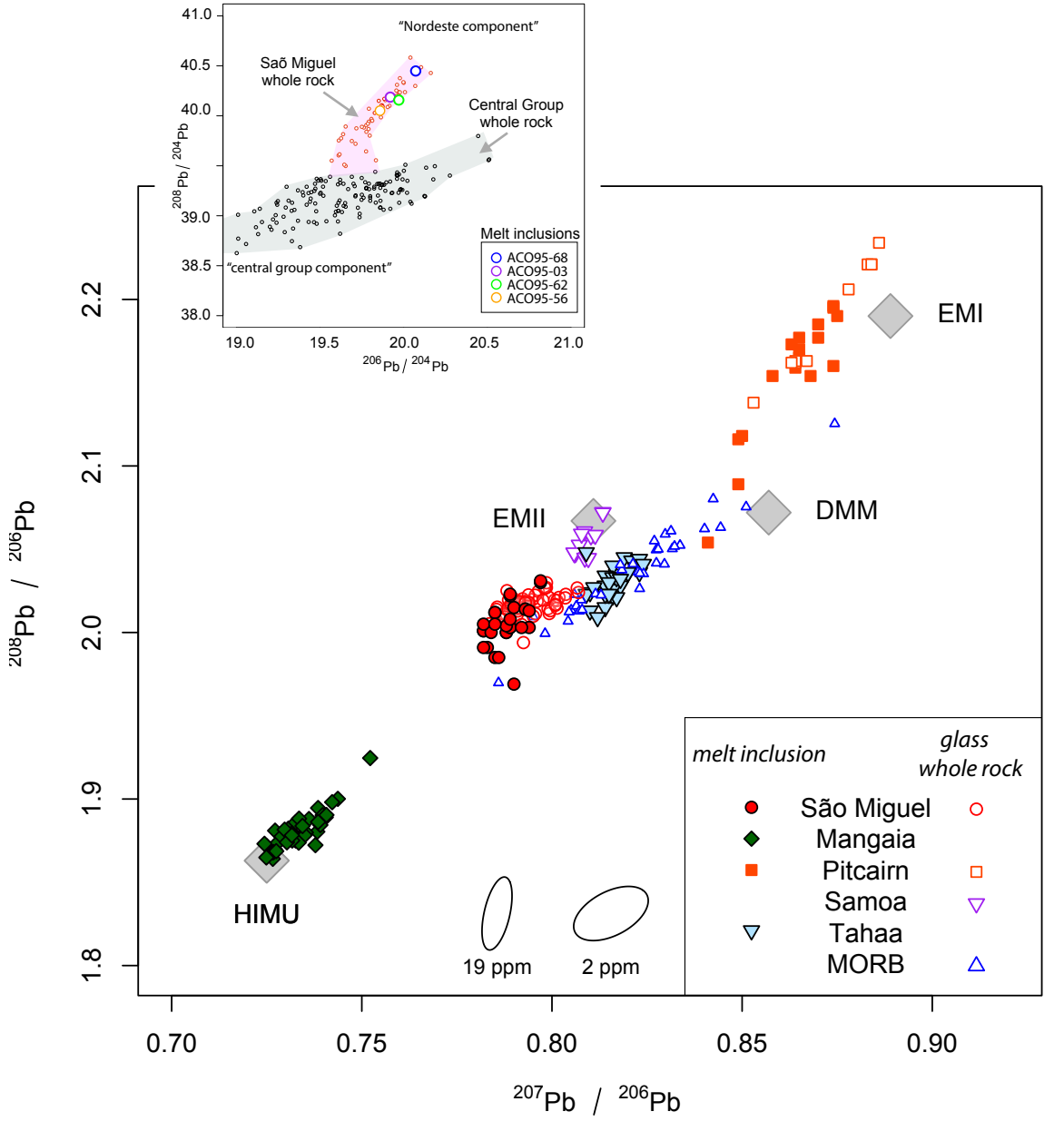
"Nordeste component"
Saõ Miguel whole rock
Central Group whole rock
"central group component"
Melt inclusions
ACO95-68
ACO95-03
ACO95-62
ACO95-56
208Pb/204Pb
206Pb/204Pb
EMI
EMII
DMM
HIMU
melt inclusion
glass
whole rock
São Miguel
Mangaia
Pitcairn
Samoa
Tahaa
MORB
19 ppm
2 ppm
208Pb / 206Pb
207Pb / 206Pb

Figure6

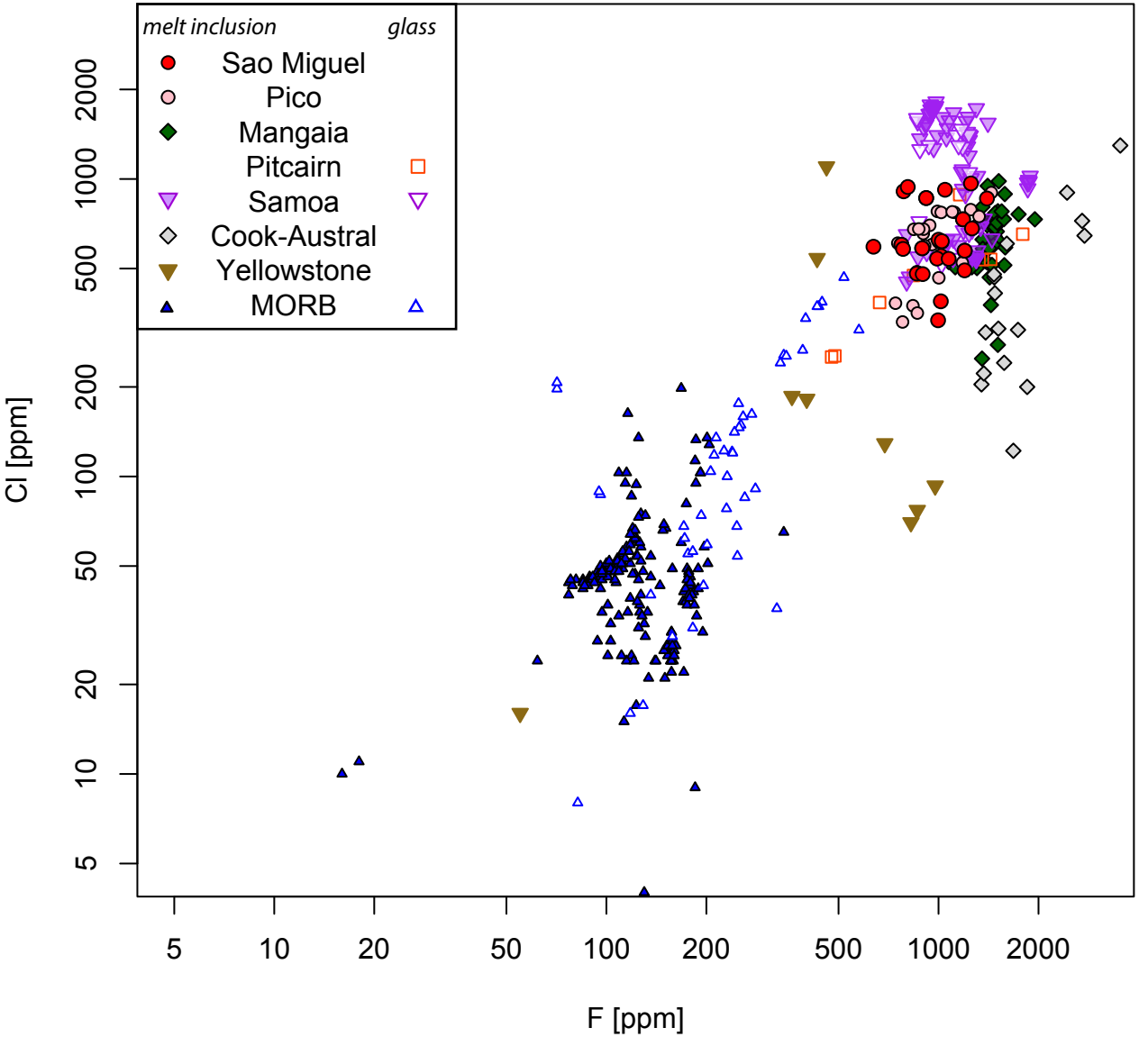
melt inclusion
glass
Sao Miguel
Pico
Mangaia
Pitcairn
Samoa
Cook-Austral
Yellowstone
MORB
Cl [ppm]
5
10
20
50
100
200
500
1000
2000
F [ppm]
5
10
20
50
100
200
500
1000
2000

Figure7

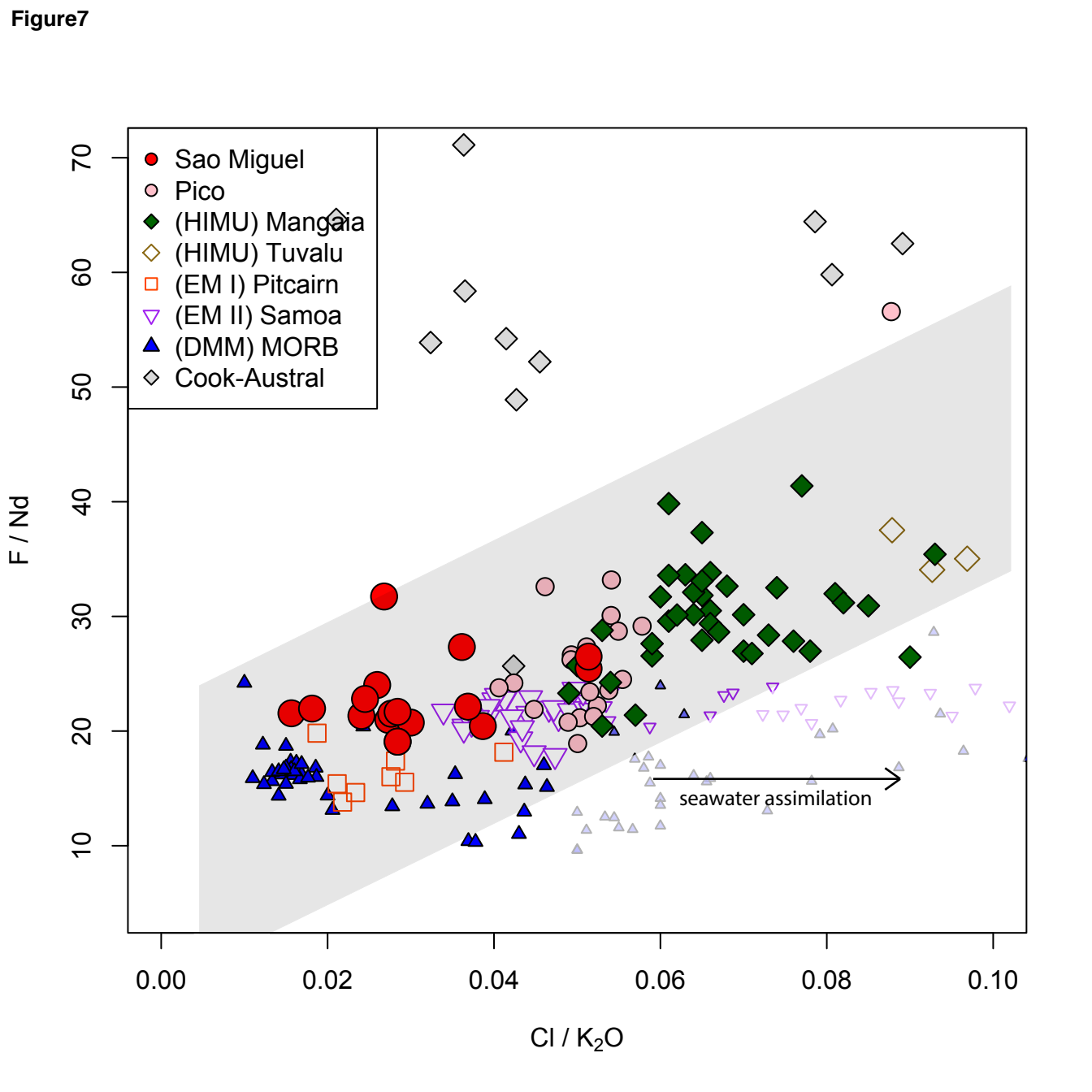
Sao Miguel
Pico
(HIMU) Mangaia
(HIMU) Tuvalu
(EM I) Pitcairn
(EM II) Samoa
(DMM) MORB
Cook-Austral
seawater assimilation
F / Nd
Cl / K2O
10
20
30
40
50
60
70
0.00
0.02
0.04
0.06
0.08
0.10

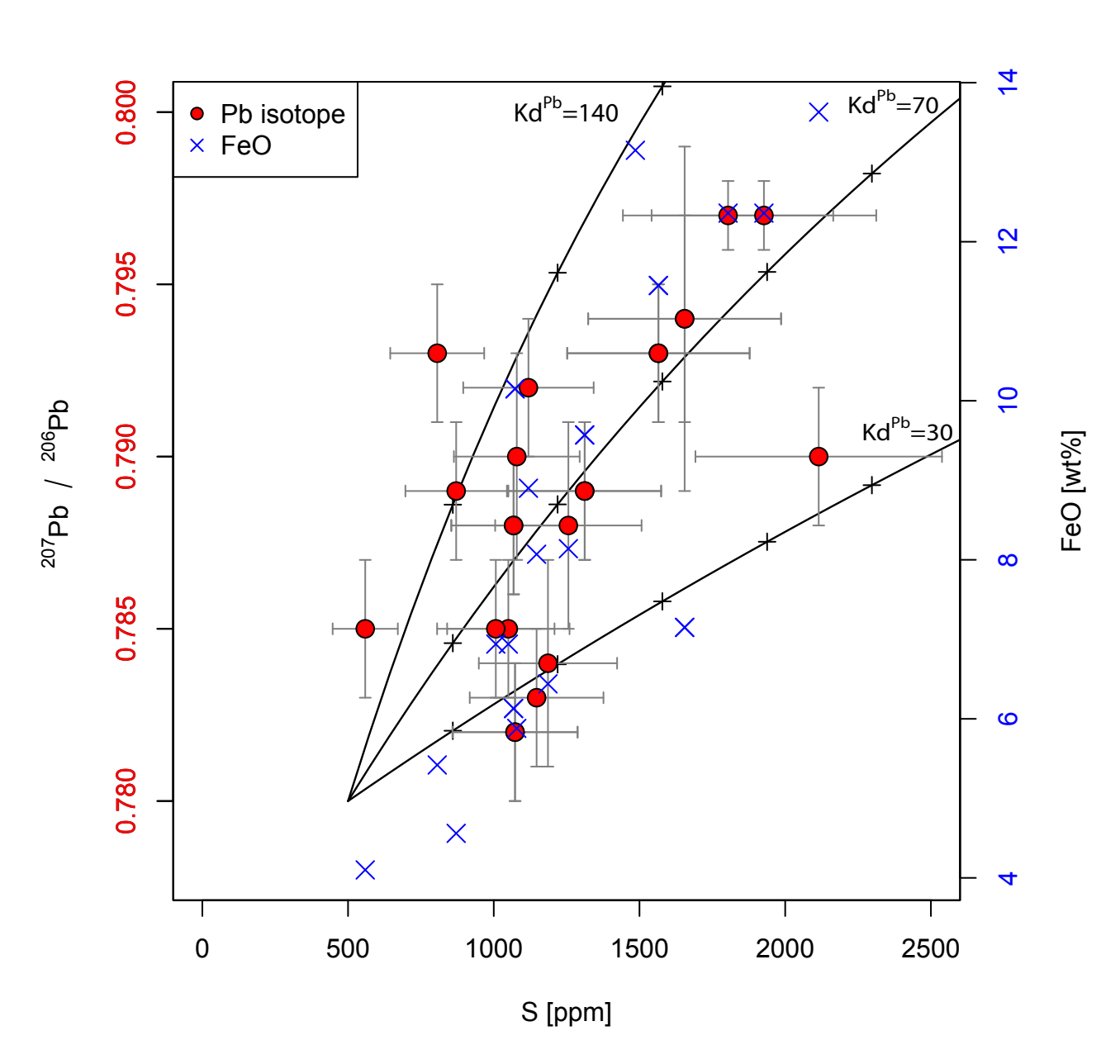
Pb isotope
FeO
Kd^Pb=140
Kd^Pb=70
Kd^Pb=30
0.800
0.795
0.790
0.785
0.780
207Pb / 206Pb
14
12
10
8
6
4
FeO [wt%]
0
500
1000
1500
2000
2500
S [ppm]

Figure9

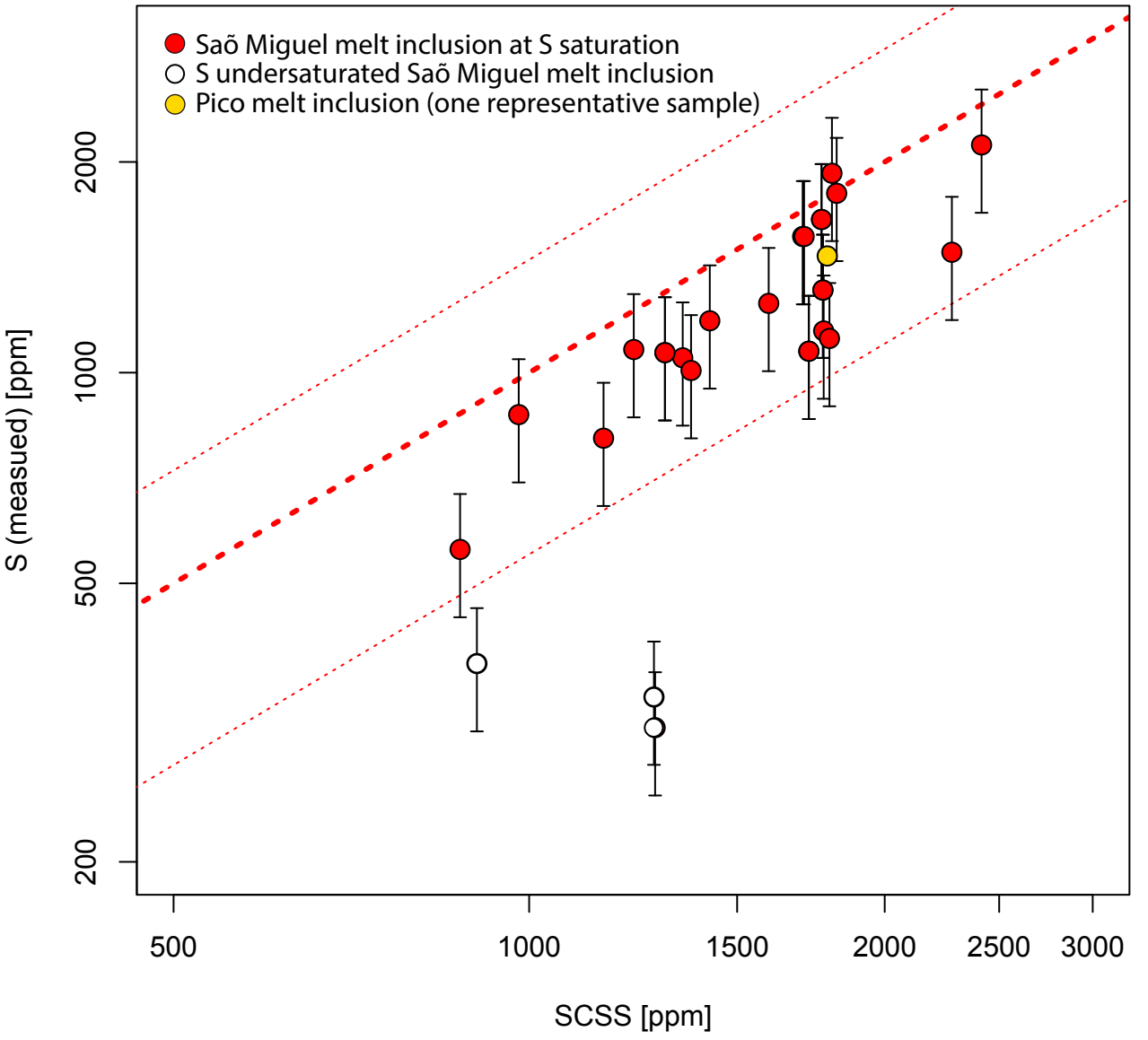
Saõ Miguel melt inclusion at S saturation
S undersaturated Saõ Miguel melt inclusion
Pico melt inclusion (one representative sample)
S (measued) [ppm]
200
500
1000
2000
SCSS [ppm]
500
1000
1500
2000
2500
3000

Figure10

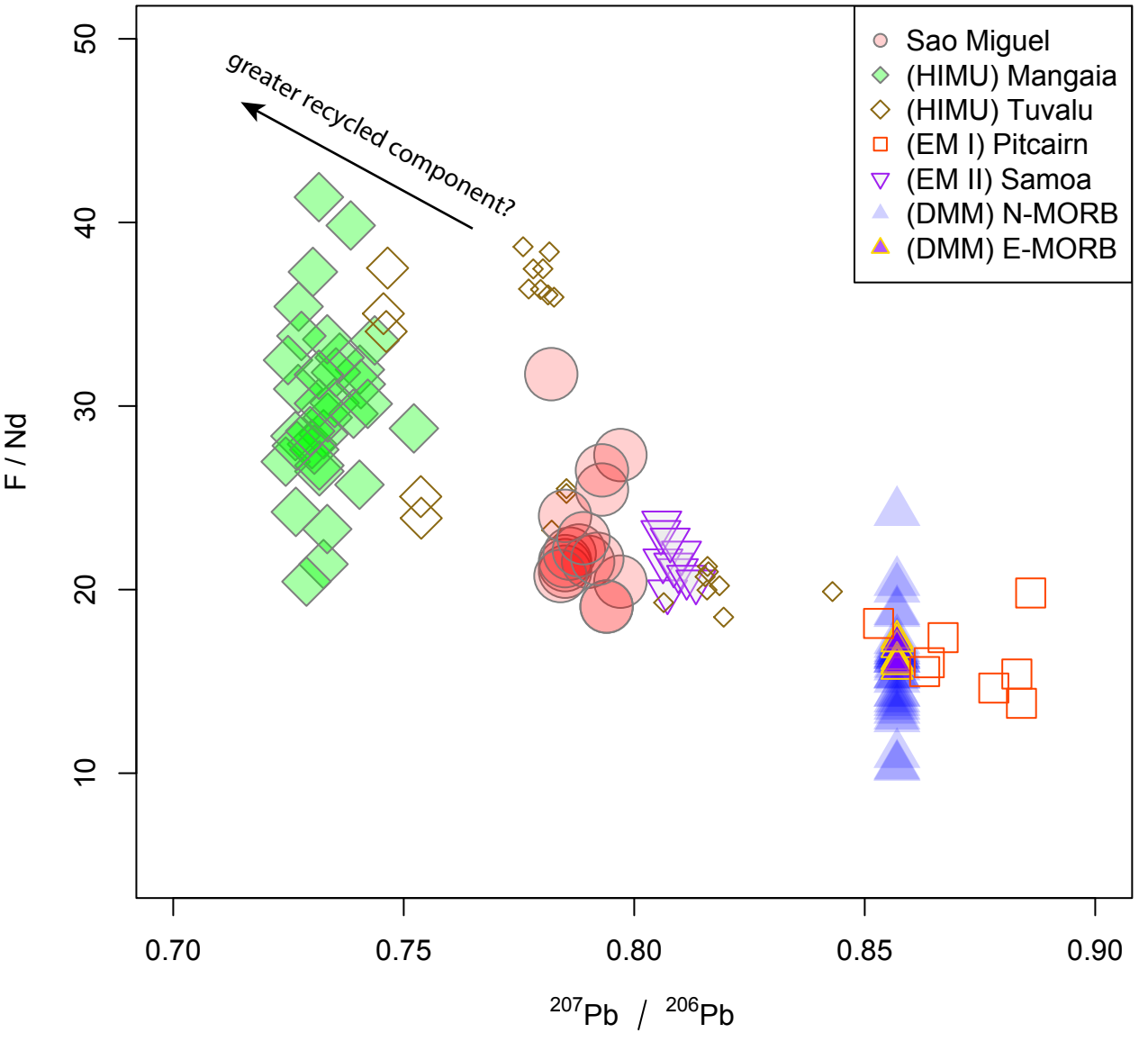
Sao Miguel
(HIMU) Mangaia
(HIMU) Tuvalu
(EM I) Pitcairn
(EM II) Samoa
(DMM) N-MORB
(DMM) E-MORB
greater recycled component?
F / Nd
10
20
30
40
50
0.70
0.75
0.80
0.85
0.90
207Pb / 206Pb

Table1

Click here to download Table: Table 1.pdf

Table 1: Volatile elements (CO_2, H_2O, F, S, Cl) and Pb isotope compositions of 19 homogenized olivine–hosted melt inclusions and Pb-isotope compositions of 4 whole rocks from Sao Miguel, Azores. The saturation pressure of CO_2-H_2O is given in MPa.

Name	CO_2 $\mu g.g^{-1}$		H_2O $\mu g.g^{-1}$		F $\mu g.g^{-1}$		S $\mu g.g^{-1}$		Cl $\mu g.g^{-1}$		$^{207}Pb/^{206}Pb$		$^{208}Pb/^{206}Pb$		$^{206}Pb/^{204}Pb$		$^{207}Pb/^{204}Pb$		$^{208}Pb/^{204}Pb$		$^{\#}$P sat MPa
ACO95-3a	1078	18	107	86	1017	11	1050	17	551	12	0.785	0.002	2.012	0.004	19.437	0.146	15.353	0.117	39.309	0.304	142
duplicate	n.d.		n.d.		1000	47	1007	23	625	42	0.785	0.002	2.012	0.003	19.450	0.165	15.382	0.136	39.360	0.337	
ACO95-3b	n.d.		n.d.		893	131	1068	39	585	20	0.788	0.002	2.000	0.005	19.729	0.169	15.634	0.126	39.655	0.329	
duplicate	n.d		nd.		n.d.		n.d.		n.d.		0.788	0.002	2.000	0.004	19.652	0.186	15.585	0.143	39.479	0.371	
ACO95-56a*	n.d.		n.d.		637	98	2115	56	592	42	0.790	0.002	2.015	0.003	19.692	0.108	15.675	0.091	39.896	0.230	
ACO95-56c	n.d.		n.d.		785	95	1147	60	909	36	0.783	0.002	1.991	0.005	20.027	0.222	15.785	0.172	40.019	-	
ACO95-56e	n.d.		n.d.		773	216	1312	17	601	39	0.789	0.002	2.022	0.004	19.877	0.160	15.795	0.126	40.422	0.340	
duplicate	n.d.		n.d.		n.d.		n.d.		n.d.		0.789	0.002	2.023	0.004	19.837	0.142	15.765	0.114	40.323	-	
ACO95-56f	1035	14	684	17	1399	10	1927	11	860	10	0.797	0.001	2.030	0.003	19.346	0.124	15.617	0.103	39.732	0.239	119
duplicate	n.d.		n.d.		1046	69	1804	16	920	49	0.797	0.001	2.031	0.003	19.468	0.136	15.635	0.114	39.763	0.275	
ACO95-56g	n.d.		n.d.		1185	95	1073	35	732	60	0.782	0.002	2.001	0.004	19.886	0.154	15.682	0.121	40.044	0.282	
duplicate	n.d.		n.d.		n.d.		n.d.		n.d.		0.782	0.002	2.001	0.007	19.926	0.184	15.698	0.139	40.077	0.371	
ACO95-62b*	n.d.		n.d.		782	94	806	6	582	43	0.793	0.003	2.007	0.006	20.083	0.301	16.035	0.236	40.508	0.551	
ACO95-62c*	n.d.		n.d.		808	96	1486	31	940	38	n.d.	n.d.	n.d.	n.d.	n.d.	n.d.	n.d.	n.d.	n.d.	n.d.	
ACO95-62d*	1097	11	1286	10	918	5	1565	6	863	4	0.793	0.002	2.014	0.003	19.546	0.136	15.596	0.109	39.552	0.249	142
duplicate	n.d.		n.d.		n.d.		n.d.		n.d.		0.793	0.002	2.014	0.003	19.549	0.153	15.614	0.116	39.579	0.300	
ACO95-62h	725	90	1552	24	860		1079		481		0.790	0.003	1.969	0.008	n.d.	n.d.	n.d.	n.d.	n.d.	n.d.	118
ACO95-62i	77	5	1359	24	997	11	344	3	335	7	0.785	0.003	1.985	0.006	19.968	0.234	15.797	0.190	39.777	0.420	12
duplicate	n.d.		n.d.		1016	204	311	34	388	20	0.786	0.002	1.985	0.004	19.997	0.241	15.831	0.201	39.884	0.458	
ACO95-68a	1178	36	397	6	1023	10	1186	7	618	9	0.784	0.003	2.000	0.006	19.881	0.202	15.699	0.159	40.013	0.425	148
2000-4-2	n.d.		704		1199		1655		574		0.794	0.005	2.003	0.012	19.269	0.247	15.287	0.179	38.861	0.529	
duplicate	n.d.		n.d.		n.d.		n.d.		n.d.		0.794	0.003	2.013	0.006	19.323	0.296	15.320	0.201	39.160	0.595	
2000-4-4	n.d.		n.d.		1252	134	1256	34	966	43	0.788	0.003	2.004	0.007	19.406	0.215	15.299	0.165	39.164	0.395	
2000-4-5	547	73	1164	50	1261	67	1119	41	682	40	0.792	0.002	2.003	0.004	19.753	0.231	15.648	0.185	39.843	0.441	57
2000-9-1	399	51	616	30	990	55	559	19	540	26	0.785	0.002	2.005	0.005	20.212	0.196	15.874	0.166	40.805	0.386	78
2000-9-2	705	98	805	40	1073	61	871	30	539	26	0.789	0.002	2.008	0.006	20.232	0.207	15.949	0.165	40.897	0.421	129
2000-9-4	n.d.		1206	60	1198	61	384	13	493	23	0.782	0.003	1.991	0.005	19.759	0.194	15.446	0.147	39.601	0.393	
whole rock:																					

ACO95-03	n.d.	n.d.	n.d.	0. 79017	2.01741	19.9197	15.7398	40.1871
ACO95-56	n.d.	n.d.	n.d.	0. 79158	2.01683	19.8583	15.7197	40.0516
ACO95-62	n.d.	n.d.	n.d.	0. 78801	2.01078	19.9709	15.7376	40.1577
ACO95-68	n.d.	n.d.	n.d.	0. 78561	2.01521	20.0716	15.7686	40.4488
NBS 981	n.d.	n.d.	n.d.	0. 91459	2.16707	16.9356	15.4891	36.7006

Errors on the volatile element measurements represent 1 sigma error in ppm. Errors for Pb-isotope measurements in melt inclusions represent 1 standard error of the mean. For whole rock Pb-isotope analysis an external precision inferred by repeated analysis of NBS 980 standard gives a relative 2σ error of 40, 60, 150, 160 and 170 ppm for $^{207}Pb/^{206}Pb$, $^{208}Pb/^{206}Pb$, $^{206}Pb/^{204}Pb$, $^{207}Pb/^{204}Pb$ and $^{208}Pb/^{204}Pb$, respectively (Vlastélic et al., 2009). When H_2O and CO_2 measurements are reported, the entire volatile suite (H_2O, CO_2, F, S, Cl) were done by SIMS (11 MI out of 19), and $^{\#}$the pressure of saturation H_2O-CO_2 was estimated using model Magmat Sat (Ghiorso, 2015). When "only" F, Cl and S are reported, the analysis were done by EMP. * signs the presence of a bubble in the melt inclusions.
For the plots with Pb isotopes and volatiles (Fig. 8 and 9), every "melt inclusion duplicate" was assigned the volatile values of its "parent-melt inclusion".

Table2

Click here to download Table: Table 2.pdf

Table 2: Major elements corrected compositions* of 19 homogenized olivine–hosted melt inclusions from Sao Miguel, Azores (in wt%) and size of the melt inclusions (long axis (L) and short axis (l), in μm).

	Na_2O	MgO	SiO_2	Al_2O_3	K_2O	FeO_{tot}	MnO	CaO	TiO_2	P_2O_5	Kd	Mg#	Size L x l (μm)
ACO95-03a	2.81	7.11	48.35	14.11	2.29	6.94	0.10	13.53	4.13	0.62	0.27	87.1	107 37
ACO95-03b	3.05	5.54	49.65	15.51	1.54	6.13	0.08	13.97	3.94	0.56	0.28	85.4	
ACO95-56a	1.98	16.08	42.17	11.44	1.38	13.63	0.20	8.92	3.68	0.52	0.27	88.7	
ACO95-56c	2.55	9.94	47.08	11.60	1.62	8.07	0.04	14.69	3.89	0.52	0.28	88.7	
ACO95-56e	2.64	10.12	46.60	12.32	2.04	9.57	0.14	12.31	3.62	0.65	0.27	87.5	
ACO95-56f	3.09	6.35	43.92	16.25	2.38	12.36	0.22	9.89	4.73	0.82	0.28	76.9	72.8 63.5
ACO95-56g	2.88	10.29	45.44	14.45	1.83	10.15	0.16	10.08	4.14	0.58	0.28	86.7	
ACO95-62b	2.88	4.92	50.29	15.95	2.07	5.42	0.18	13.78	3.98	0.53	0.28	85.2	
ACO95-62c	2.39	8.34	42.77	14.60	1.58	13.15	0.26	11.43	4.84	0.63	0.28	80.0	
ACO95-62d	2.84	6.94	45.09	15.80	1.68	11.45	0.07	11.65	3.94	0.54	0.28	85.4	95.6 85.2
ACO95-62h	2.88	5.67	49.63	15.61	1.74	5.88	0.08	14.11	3.90	0.50	0.28	86.1	96.2 93.2
ACO95-62i	2.99	6.01	48.87	15.85	2.14	6.33	0.03	12.47	4.41	0.91	0.28	86.1	83.1 74.1
ACO95-68a	2.73	7.91	48.49	13.13	2.06	6.44	0.10	14.34	4.15	0.66	0.28	88.8	
2000-4-2	2.51	4.46	44.47	15.55	2.02	7.15	0.13	15.95	7.10	0.66	0.27	80.4	
2000-4-4	3.13	6.04	46.14	14.60	2.62	8.14	0.08	13.19	5.32	0.73	0.27	83.1	
2000-4-5	2.96	5.48	44.98	14.56	2.40	8.90	0.15	13.93	5.89	0.78	0.27	80.4	
2000-9-1	3.03	3.42	53.03	17.32	2.08	4.10	0.04	12.65	3.84	0.49	0.28	83.9	
2000-9-2	3.23	3.36	51.17	17.52	2.20	4.56	0.11	12.88	4.30	0.69	0.28	82.2	
2000-9-4	3.75	3.17	52.98	18.31	1.84	4.29	0.15	11.53	3.31	0.68	0.28	82.6	

* Reported values are corrected for olivine post-entrapment crystallization, and normalized to 100% on a volatile-free basis. Uncertainty is not assessed since the accuracy is olivine correction model dependent. Precision is proportionally equal to electron microprobe measurements (see electronic annex.)

Table3

Click here to download Table: Table 3.pdf

Table 3: Trace elements corrected compositions* (in $\mu g.g^{-1}$) of homogenized 12 olivine–hosted melt inclusions from Sao Miguel, Azores.

	Rb	Sr	Y	Zr	Nb	Ba	La	Ce	Nd	Sm	Eu	Gd	Dy	Er	Yb	Hf	Ta	Th	U
ACO95-03a	58.8	582	25.9	296	62	442	52.2	106	48	9.5	2.7	7.7	5.6	2.38	1.89	7.10	3.64	6.94	1.89
ACO95-56f	62.4	760	26.4	315	70	556	50.2	104	51	9.7	2.9	8.1	5.9	2.61	2.04	7.79	4.16	6.04	1.63
ACO95-62d	40.7	624	20.9	208	46	424	33.5	70	36	8.3	2.7	6.6	4.4	2.10	1.32	4.93	2.52	3.65	1.20
ACO95-62h	39.3	505	27.7	255	49	365	37.8	81	40	8.1	2.5	7.7	5.8	2.99	2.45	6.73	2.78	4.22	1.12
ACO95-62i	59.7	459	31.2	314	60	442	47.6	99	46	9.3	2.8	8.6	6.3	3.14	2.50	7.69	3.57	5.72	1.57
ACO95-68a	48.3	627	24.7	300	59	434	51.4	104	49	9.4	2.7	8.4	5.8	2.45	1.93	7.45	3.60	5.78	1.54
2000-4-2	50.4	667	36.0	361	75	569	57.5	114	63	12.8	3.7	11.1	8.3	3.91	2.73	9.91	4.77	6.96	1.70
2000-4-4	66.8	777	31.3	335	75	597	56.2	119	57	11.4	3.3	10.1	7.3	3.16	2.59	8.96	4.85	6.77	1.81
2000-4-5	59.8	787	31.7	328	73	550	55.5	117	58	11.8	3.5	10.2	7.5	3.17	2.50	8.56	4.41	6.17	1.69
2000-9-1	49.4	555	29.3	248	67	424	43.4	90	41	7.4	2.2	7.0	6.1	3.15	2.63	6.39	4.16	5.71	1.39
2000-9-2	60.3	585	32.2	287	60	468	49.1	102	47	9.6	2.9	8.3	6.8	3.43	2.88	7.70	3.68	6.33	1.62
2000-9-4	52.2	528	30.5	246	56	420	40.5	83	38	8.0	2.4	7.9	6.7	3.26	2.74	6.23	3.36	5.29	1.41

* Reported values are corrected for olivine post-entrapment crystallization, and normalized to 100% on a volatile-free basis. Relative 1σ standard errors are better than 3% for Rb, Sr, Y, Zr, Nb, Ba, La, Ce, less than 4% for Nd, better 9% for Sm, Eu, Gd, Dy, Er, Hf, Ta, Th and U, and 12% for Yb. Measurements of samples that are not presented here were attempted, but failed due to the lack of inclusion volume.

Table supplementary material

Click here to download Table: -revised Suppl Material.xlsx

Table 1A: Major elements compositions of 19 olivines from Sao Miguel, Azores (in wt%).

	MgO	SiO2	Al2O3	FeO	Mno	CaO
ACO95-03a	45.95	41.11	0.03	12.15	0.17	0.29
ACO95-03b	45.92	39.68	0.03	13.94	0.20	0.26
ACO95-56a	47.20	40.16	0.04	10.69	0.15	0.30
ACO95-56c	48.08	39.87	0.04	10.89	0.13	0.29
ACO95-56e	47.63	40.08	0.02	12.08	0.21	0.28
ACO95-56f	39.28	38.28	0.04	21.01	0.27	0.21
ACO95-56g	46.37	39.70	0.05	12.67	0.17	0.28
ACO95-62b	44.99	40.00	0.04	13.94	0.18	0.30
ACO95-62c	40.91	38.75	0.04	18.24	0.24	0.24
ACO95-62d	45.08	39.55	0.05	13.76	0.21	0.28
ACO95-62h	46.34	39.90	0.03	13.35	0.19	0.28
ACO95-62i	46.34	39.90	0.03	13.35	0.19	0.28
ACO95-68a	48.35	39.26	0.05	10.89	0.16	0.25
4/2/2000	41.79	39.15	0.00	18.20	0.29	0.36
4/4/2000	43.68	39.64	0.02	15.80	0.34	0.34
4/5/2000	41.99	39.81	0.00	18.26	0.23	0.54
9/1/2000	44.01	40.03	0.00	15.08	0.20	0.31
9/2/2000	42.72	39.47	0.00	16.53	0.17	0.28
9/4/2000	43.73	40.45	0.00	16.37	0.15	0.27

Table 1B: Major elements uncorrected compositions of 19 homogenized olivine–hosted melt inclu

	Na2O	MgO	SiO2	Al2O3	K2O	FeO
ACO95-03a	2.58	10.02	47.49	12.96	2.10	7.29
ACO95-03b	2.62	10.72	47.75	13.31	1.33	7.07
ACO95-56a	2.34	9.58	41.83	13.52	1.63	13.98
ACO95-56c	2.38	11.29	45.60	10.83	1.51	7.99
ACO95-56e	2.28	14.45	45.06	10.64	1.76	9.72
ACO95-56f	2.93	7.42	42.91	15.37	2.25	12.44
ACO95-56g	3.09	7.14	45.37	15.48	1.96	9.81
ACO95-62b	2.50	9.67	48.45	13.85	1.79	6.38
ACO95-62c	2.36	7.94	41.88	14.39	1.56	12.83
ACO95-62d	2.75	7.67	44.53	15.32	1.63	11.38
ACO95-62h	2.50	10.76	48.04	13.53	1.50	6.78
ACO95-62i	2.77	8.62	47.90	14.68	1.98	6.74
ACO95-68a	2.52	10.11	47.06	12.13	1.91	6.58
4/2/2000	2.19	8.73	43.34	13.56	1.76	8.35
4/4/2000	2.94	8.03	45.45	13.71	2.46	8.49
4/5/2000	2.70	8.03	44.00	13.31	2.19	9.45
9/1/2000	2.53	9.89	50.70	14.47	1.73	5.83